



RESEARCH UNIVERSITY PARIS



PhD manuscript

Etienne Bonnassieux

March 27, 2018

Supervisors: Philippe Zarka, Oleg Smirnov, Cyril Tasse

Title

title goes here



Contents

	Page
1 Introduction	1
1.1 This Manuscript	1
1.2 Overview of Radio Interferometric Techniques	1
1.3 A Brief Introduction to Radio Astronomy	1
1.4 Interferometry: Bypassing the Diffraction Limit	2
1.4.1 The Baseline	3
1.4.2 The Visibility	3
1.4.3 The uv -plane	4
1.4.4 The Point-Spread Function	5
1.4.5 From Dirty to Clean: Mitigating the PSF	6
1.5 Calibration Methods in Radio Interferometry	7
1.5.1 Generational Analysis	8
1.6 The Low- ν Sky: Emission Mechanisms	10
1.6.1 Thermal Radiation	10
1.6.2 Free-Free Radiation	10
1.6.3 Synchrotron Radiation	10
2 Introduction to Mathematical Framework: the RIME Formalism	11
2.1 Setting up the RIME: a single point source	11
2.2 Expanding our Jones Chain	12
2.2.1 Geometric Effects: the Phase Delay Jones Matrix	13
2.2.2 The Coherency Matrix	13
2.3 Multiple Point Sources	14
2.4 Diffuse Emission: the Full-sky RIME	14
2.4.1 Deriving the Fully-Sky RIME	14
2.4.2 Recovering the van Cittert-Zernike Theorem	15
2.5 Time-dependent Jones matrices, Smearing, and Decoherence	16
2.5.1 Time-dependence of Jones matrices	16
2.5.2 Smearing and Decoherence	16
2.6 Noise	18
3 Analysing the Variance of Gain Solutions	19
3.1 Foreword	19
3.2 Introduction	19
3.3 Building the Noise Map	23
3.3.1 The Cov-Cov Relationship in the $\delta u \delta v$ plane	23

3.3.2	Statistical Analysis	25
3.3.3	Noise Map Simulations	28
3.4	Adaptive Quality-based Weighting Schemes	31
3.4.1	Optimising sensitivity	32
3.4.2	Minimising Calibration Artefacts	33
3.5	Estimating the Covariance Matrix	33
3.5.1	Baseline-based Estimation	33
3.5.2	Antenna-based Estimation	35
3.6	Applying the Correction to Simulated Data	36
3.7	Applying the Correction to Real Data	38
3.8	Discussion	40
4	Scientific Strategy	43
4.1	Science Goal	43
4.2	3C295 and the Extended Groth Strip	44
4.3	Imaging the Full Primary Beam	45
4.4	Test Decorrelation	45
4.5	Imaging the EGS with LOFAR international stations	45
4.5.1	Science Goals	45
5	High-resolution Imaging of 3C295	47
5.1	Aims & Methodology	47
5.2	Data Reduction	47
5.2.1	Data & Observation Properties	47
5.2.2	Calibrating the Data	48
5.3	Overlays & Spectral Analaysis	52
5.3.1	Overlays of 3C295 at Multiple Frequencies	52
5.3.2	Spectral Analaysis	52
6	Imaging the Extended Groth Strip without International Stations	55
6.1	Aims & Methodology	55
6.2	Data Reduction	55
6.2.1	Data & Observation Properties	55
6.2.2	Calibration Strategy	56
6.3	Overlays & Images	56
7	Imaging the Extended Groth Strip with the full LOFAR array	57
7.1	Aims & Methodology	57
7.2	Testing Decorrelation - LOBOS Sources in the Primary Beam	58
7.3	Patchwise Imaging of the EGS using LOFAR International Stations	58
8	Conclusion & Future Work	59
	Bibliography	62

Chapter 1

Introduction

1.1 This Manuscript

write introduction to the thesis

1.2 Overview of Radio Interferometric Techniques

In this section, we will cover the difficulties introduced by the combination of sparse uv -coverage and weak *a priori* constraints on the sky brightness distribution. While we do not need to strictly base ourselves on the RIME formalism described in Chapter 2, it remains the conceptual framework we will assume that the reader uses. For the remainder of this section, we will assume that calibration has been successfully carried out, and that we are working on the *corrected visibilities*, i.e. gain-corrected visibilities.

We will begin by linking interferometry to more concrete concepts: specifically, we will give a (very!) brief introduction to radio antennas and their characteristics. This will make the ideas and basis of radio interferometry more accessible by allowing us to explain the abstractions that interferometry relies on in terms of simpler instrumental configurations. We will then introduce the concrete problems that interferometry introduces: both a recapitulation of the venerable Zernike-van Cittert theorem (cf. van Cittert 1934) and the problem of incomplete uv -coverage.

1.3 A Brief Introduction to Radio Astronomy

Radio astronomy consists of observing the electromagnetic field at very long wavelengths, which means using radio dishes. These dishes measure a voltage signal, proportional to variations in the electromagnetic field in the direction of sensitivity. Achieving good sensitivity with radio dishes means having a very large collecting area - in this respect, they behave exactly the same way as optical telescopes. Similarly, when well-designed, they are diffraction-limited - this means that, once again like optical telescopes, their resolution is limited by their diameter.

However, because radio frequencies are so much lower, achieving a resolution comparable to e.g. the HST requires extremely large dishes. While there exist telescopes, both

old and new, which work on this principle (from Arecibo Observatory, shown in Fig. , to the upcoming FAST telescope in China, shown in Fig.)

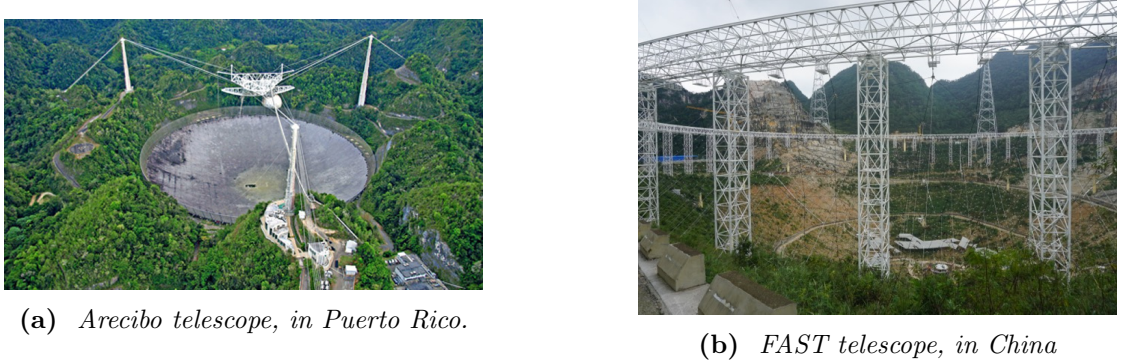


Figure 1.1. Examples of large single-dish radio telescopes.

Calibrating these dishes is a relatively straightforward matter - the signal loss and distortion as the dish converts the electromagnetic wave to a voltage can be described, based on the dish, either as a simple scaling factor, or a complex number (giving information on phase and amplitude errors). This loss and distortion model is referred to as the *antenna gain*. Solving for these using more complex interferometric array is a problem described in Section 1.5.

For the remainder of this section, we will assume that calibration has been performed perfectly, and that the gain-corrections have been applied to voltage measurements.

1.4 Interferometry: Bypassing the Diffraction Limit

There are two quantities of interest to astronomers of all stripes: sensitivity and resolution. An instrument's sensitivity is a function of its collecting area¹. Resolution, for well-designed instruments², is limited by diffraction. This introduces issues specific to the radio domain. Radio waves, however, have very long wavelengths - often comparable to meters, rather than the 100nm wavelengths of optical light. This introduces specific issues for astronomers, since achieving a resolution comparable to those of optical telescopes would require making telescopes with apertures tens of millions of times larger than those already titanic instruments!

To produce high-resolution maps of the radio sky, this technical limitation demands a technical solution. In practice, this solution consists of recourse to interferometric techniques. Indeed, interferometry can be thought of as the construction of a "sparse" dish, as illustrated in Fig.

¹It is also a function of technological factors, of course, but *ceteris paribus*, a more sensitive telescope means a telescope with a wider collecting area

²By this, we mean that we assume that an instrument strives to optimise resolution.

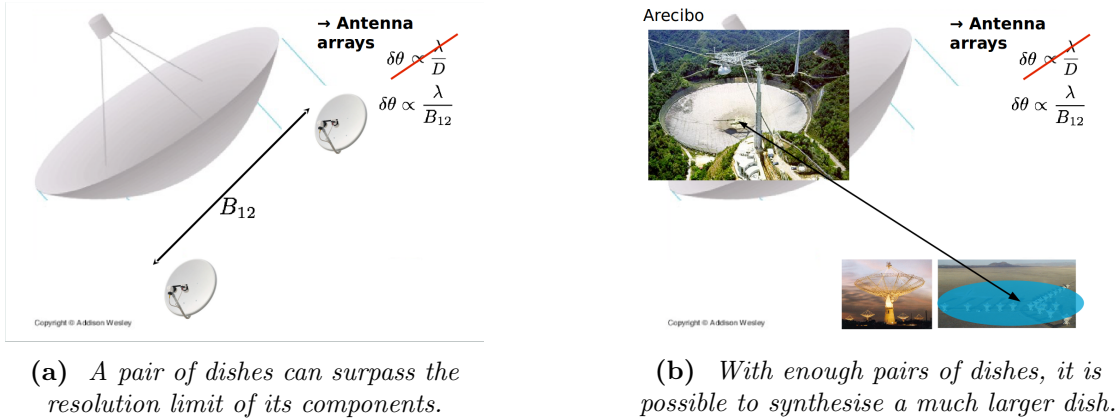


Figure 1.2. Illustration of the underlying principle of interferometry. The 27 dishes of the VLA can be thought of as "synthesising" a similar circular dish as Arecibo. This idea is the reason why radio interferometry is historically known as "aperture synthesis" in the literature of radio astronomy. Both images are copyrighted by Addison Wesley.

Of course, this improvement of resolution does not come for free. To understand the cost of interferometry, let us discuss the properties of its core component: the baseline.

1.4.1 The Baseline

To define the baseline, we must begin by considering the geometric properties of an interferometric array. For now, let us assume that we are observing the sky above the array, a practice known as drift-scanning. A baseline then consists of the vector subtraction of the positions, in 3-dimensional space, of its two constituent antennas. Note that each antenna pair therefore has 2 corresponding baselines, since for each pair of antennas A and B we have baselines AB and BA. These distance vectors are then divided by the observing wavelength to give a dimensionless set of coordinates, known as (u, v, w) . These coordinates define the baseline entirely.

1.4.2 The Visibility

We have defined what a baseline corresponds to: a vector coordinate in (u, v, w) -space. To each baseline we associate a measurement, which we call the *visibility*. The visibility associated with baseline \mathbf{b}_{AB} is created by taking the voltage measured by antenna A, multiply it by the complex conjugate of the voltage measured by antenna B, average over the correlator dump time (i.e. the time over which the measurement is made). This scalar quantity is then multiplied by the baseline position vector. In other words:

$$\mathbf{b}_{AB} = V_A V_B^* \frac{\mathbf{x}_B - \mathbf{x}_A}{\nu_{\text{obs}}} \quad (1.1)$$

So we see that a visibility is a complex vector quantity. We also see that $\mathbf{b}_{AB} = \mathbf{b}_{BA}^*$: the information of the visibility associated with baseline BA is contained in the visibility associated with baseline AB. This means that in practice, only half of the visibilities ever need be stored. What does the visibility measurement correspond to?

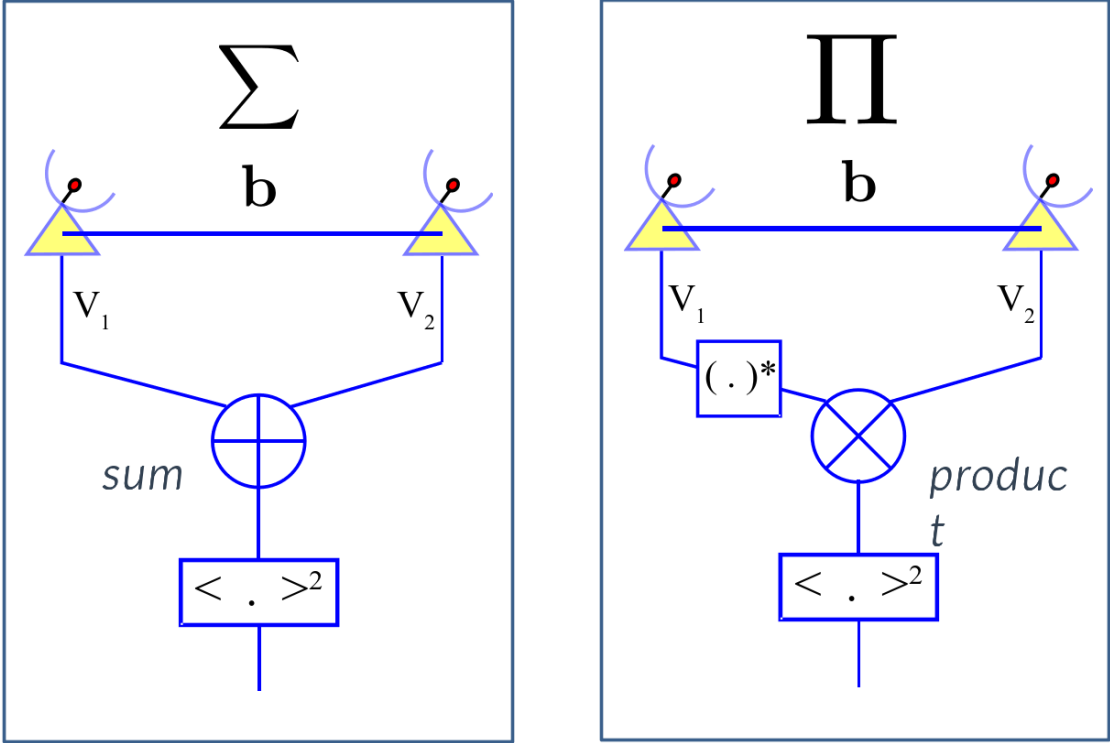


Figure 1.3. There are two ways to combine the voltages from two antennas into a visibility: they are sum-correlation and π -correlation. In this manuscript, we will only concern ourselves with the latter. Image credit: Julien Girard

The signals from various sources are additive in both antennas. Provided that the signal from both sources is coherent when observed by the dishes, the correlation between the total voltages will simply be the sum of the voltage correlations associated with individual sources - i.e. the interferometric signal from different sources are additive.

Note that in Fig. 1.4, neither source is at the zenith. We thus see that the *effective baseline* which sees each source is in fact shorter than the *physical baseline*. This can be corrected by digitally adding a phase delay in each antenna (or, in older interferometers, by playing with the cable length between each dish and the correlator) - this is in fact how interferometric arrays are pointed.

1.4.3 The *uv*-plane

In general, interferometric design is such that the *w* component of visibilities' (*u, v, w*) coordinates is negligible (or can be put in a frame of reference where it can usually be approximated as such). Radio astronomers tend to thus talk of a *uv*-plane rather than *uvw*-space to describe the space where visibilities live. The set of *uv*-values for all the baselines of an interferometric array is known as its *uv*-coverage, and defines the array's properties entirely.

For the VLA, for example, the *uv*-coverage when observing the zenith will be as shown in Fig. 1.5.

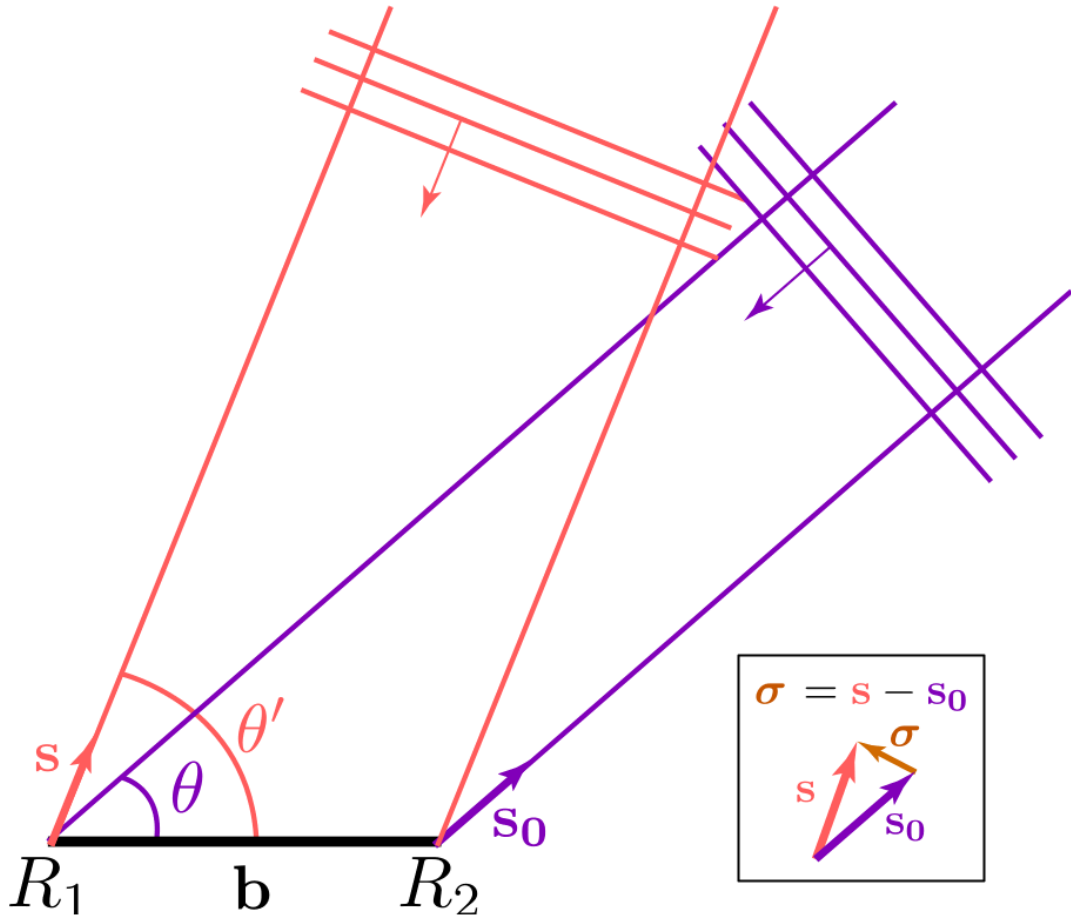


Figure 1.4. Here, we assume that there are only two sources in the sky whose signal can be measured by our antennas. The final visibility is the sum of the visibilities associated with each individual source. Image credit: Julien Girard

Individual antennas of an array can be pointed mechanically, and so the impact of pointing the interferometric array in a given direction can be minimised. But what happens to the array itself? It is useful here to go back to the illustration of Fig. 1.2b. Think of each dish in the array representing a "filled" segment of a massive but empty dish. By projecting our observation in a given direction, this dish goes from circular to elliptical.

1.4.4 The Point-Spread Function

So far, we have seen that the purpose of an interferometric array is to overcome the diffraction limit of single-dish antennas. We have described visibilities, which are the quantities measured by an interferometric array. What remains is to describe how these measurements are used to make images of the sky.

Assuming that all the antennas in an array are equivalent and perfectly calibrated, the van Cittert-Zernike theorem ((van Cittert 1934), covered in (Thompson et al. 2001)) allows us to equate a visibility with a single Fourier mode of the plane tangent to the

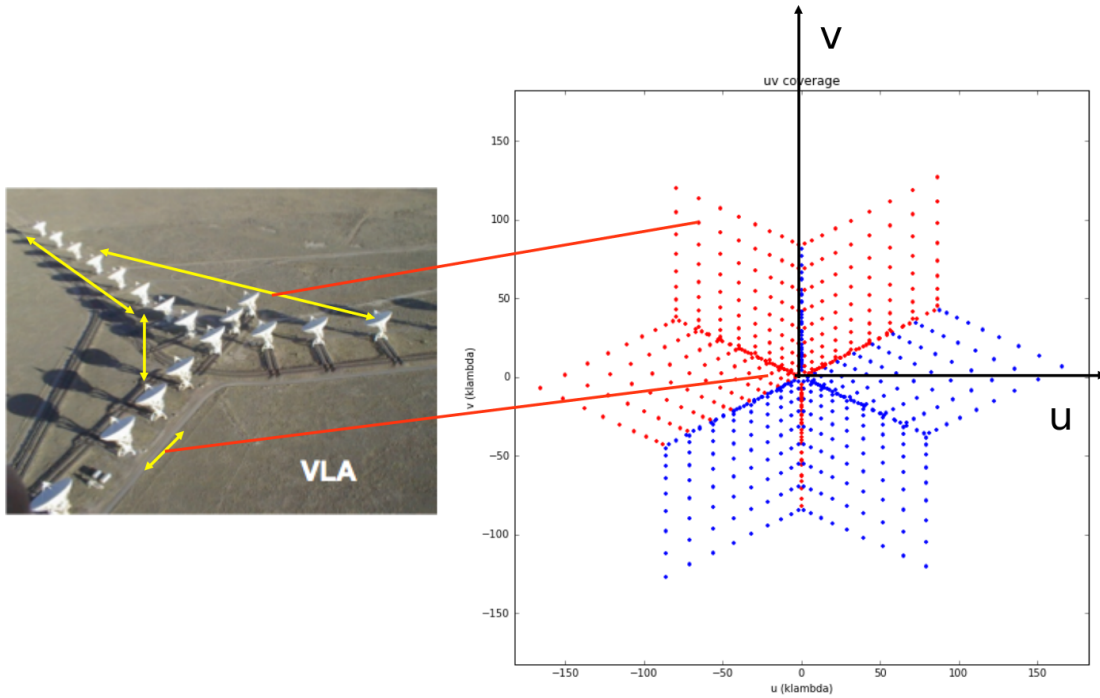


Figure 1.5. The VLA contains 27 radio dishes placed as shown above. Each antenna pair between those 27 gives two single baselines, here, one red and one blue. Image credit: Julien Girard

sky where the instrument is pointed. This direction is called the *phase centre*, because digital phase shifts are introduced between antenna voltages before averaging so as to point each visibility in this direction.

1.4.5 From Dirty to Clean: Mitigating the PSF

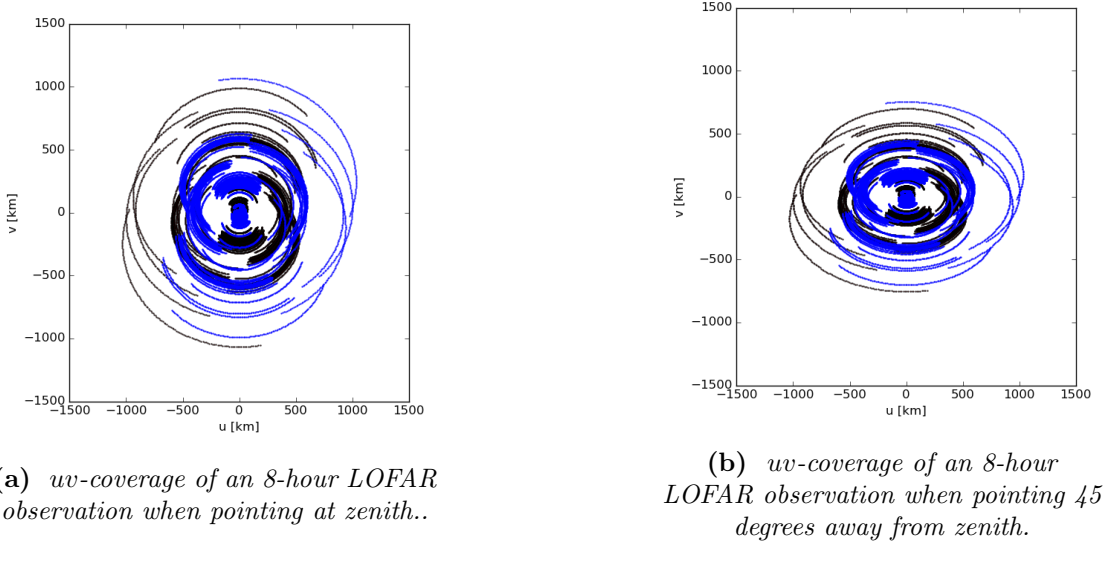


Figure 1.6. *Effect of array pointing on uv-coverage. By pointing the array 45 degrees in the v-axis, the array’s uv-coverage (and thus maximum resolution) is decreased along the v-axis.*

1.5 Calibration Methods in Radio Interferometry

In this section, we will discuss the implementation of interferometric array calibration. Our analysis is based on the RIME formalism, described in Chapter 2. One key metric of calibration quality is the *dynamic range* (DR). High dynamic ranges mean that a high contrast has been obtained, and fainter sources can be reached. Dynamic range is defined as the following:

$$DR = \frac{flux_{max}}{\max(\sigma_{thermal}, \sigma_{artefacts})} \quad (1.2)$$

where $flux_{max}$ is the flux of the brightest source, $\sigma_{thermal}$ the thermal noise in the image, and $\sigma_{artefacts}$ the noise associated with calibration artefacts.

The distinction between these two noise sources is crucial; one can never go ‘below noise’ for a given observation, no matter the quality of calibration. Astronomers typically observe for longer periods of time in order to reduce $\sigma_{thermal}$ in their images, but this will not reduce the artefacts caused by poor calibration solutions. However, uncorrected Direction-Dependent Effects will not go away on their own, no matter how long the integration time.

There are three ‘generations’ of calibration methods, of increasing complexity. I shall describe them in terms of the RIME, showing how each generation increases in generality to account for more exotic effects. For the sake of clarity, I shall henceforth refer to them interchangeably as ‘nth-generation calibration’ or ‘nGC’ methods.

1.5.1 Generational Analysis

First-Generation: Open-Loop Calibration

First-generation calibration methods (1GC methods) consist of open-loop calibration. This relies entirely on instrument stability, and thus imposes significant design constraints on radio telescopes. It consists of briefly observing a calibrator before and after each observation run to find a gain factor and offset error³

Phase calibration in the 1GC era ‘proper’ was not done, as engineers were capable of ensuring phase stability in contemporary interferometers. Phase was thus calculated relative to a fixed frame of reference, usually the central antenna of a 3-antenna array.

In RIME terms, this consists of solving for a very basic form of \mathbf{G}_p :

$$\mathbf{G}_p = [a_p t + b_p] \quad (1.3)$$

where a_p, b_p are constants solved for during open-loop calibration and t is time.

While values for a_p and b_p can in theory be found for both autocorrelation and both crosscorrelations, low signal-to-noise means that in practice, a single set of values is solved for per antenna⁴. With these techniques, one can achieve dynamic ranges of about 100:1 ((Noordam & Smirnov 2010)).

Second-Generation: Self-Calibration

Second-generation calibration methods (2GC methods) are defined by their use of *self-calibration*⁵, commonly referred to as *self-cal* ((Pearson & Readhead 1984)). As described in Section 2.4.2, this method can only be deployed if the brightness matrix of the sky is the same for all baselines⁶ (i.e. that we are not affected by direction-dependent effects).

The seeds of self-calibration (and adaptive optics) is a paper published in the era of 1GC by Jennison ((Jennison 1958), expanding on his PhD work, which was published in 1951). With sufficient signal-to-noise, he showed that *phase closure* could be calculated and errors due to the atmosphere thus mitigated.

Self-calibration and adaptive optics are the same thing, albeit meeting different constraints. Most notably, interferometric data is digital, allowing radio astronomers to perform their adaptive optics correction after the observation.

[TODO: put adaptive optics diagram here maybe]

³For a concrete example, see here.

⁴This reduces calibration to solving only for the intensity gains: the data can then only be used for *intensity mapping* (e.g. (Jennison 1957)). This practice therefore precludes polarimetry.

⁵On the discovery of self-calibration and its evolution in parallel to adaptive optics, I highly recommend the chapter titled “The Almost Serendipitous Discovery of Self-Calibration” in ”(Kellerman & Sheets 1984).

⁶This is not to say that the brightness matrix must contain only point sources, but rather that moving our interferometer 500m to the East should not change its measured visibilities

If amplitude and phase gains can be written as antenna-dependent, then each antenna-based error is estimated N times (once per baseline which includes this antenna). By estimating, and correcting for, these errors, one can use a simple source model to infer an improved one. This is why the method is referred to as self-cal; by calibrating ‘on’ a good calibrator source (bright, compact and unresolved), one can drastically improve one’s source model, along with one’s calibration solutions.

By extending this idea to VLBI⁷, *amplitude closure* was introduced to the field along with phase closure (as described in Rogers et al. 1983). Astronomers were quick to apply these methods to interferometers in general.

The great advantage of radio interferometry over optics, however, is that we can *iterate* over progressively improved source models. This is because interferometric data is digital, and because we record phase information.

In practice, of course, self-cal will be limited by noise. More precisely, it will be limited by sensitivity, in the form of the signal-to-noise ratio (henceforth SNR). For sufficiently bright sources, with high SNR, self-calibration can easily improve dynamic range by a factor of 10 (Kellerman & Sheets (1984), p. 154) in a single iteration.

Third-Generation: Direction-Dependent Effects

Third-generation calibration (3GC) is an extension of 2GC calibration which takes direction-dependent effects into account. At the time of writing, this is the cutting edge in radio interferometric calibration.

In this section, I will discuss the approach taken by [cite DDF and kMS paper when it comes out] and [cite prefactor paper if/when it is out], *facet-based calibration*. This method has an imaging equivalent (see Tasse et al. 2017, and associated papers). The approach cannot be divorced from imaging, for the simple reason that solving for and applying Jones matrices in different directions requires image-plane knowledge of the sky brightness distribution \mathbf{B} . The imaging challenges this methods introduces will be discussed in [href to relevant imaging section].

The crucial insight of this approach consists

⁷e.g. (Rogers et al. 1974)

1.6 The Low- ν Sky: Emission Mechanisms

This section aims to bring a brief introduction to the emission mechanisms which dominate in the low-frequency sky, and thus of the kind of sources visible to astronomers working in this band. write introduction to scientific stuff (e.g. synchrotron radiation, extragalactic fields, etc)

1.6.1 Thermal Radiation

dust & protoplanetary disks

1.6.2 Free-Free Radiation

bremsstrahlung

1.6.3 Synchrotron Radiation

magnetobremsstrahlung

Chapter 2

Introduction to Mathematical Framework: the RIME Formalism

In this section, we introduce the mathematical framework which forms the basis for our algorithmic work. While radio interferometry has historically been a complex business ((Thompson et al. 2001)), modern radio interferometry is based on the Radio Interferometer’s Measurement Equation, a powerful and elegant formalism which underpins modern calibration and imaging algorithms. In this section, I will give a simplified account of this formalism as described in (Smirnov 2011a) and its companion papers¹. This will form the theoretical basis on which further sections will expand. I cannot overstate the importance of the RIME as the foundation of modern calibration and imaging algorithms.

For a mathematically rigorous description of the RIME, the references used in this work (particularly (Smirnov 2011c) and (Smirnov 2011d)) are obviously the first place to look. We frame the RIME in the continuity of previous theoretical frameworks of radio interferometry, while also describing it in the context of contemporary software packages and algorithmic tools.

2.1 Setting up the RIME: a single point source

The Radio Interferometer’s Measurement Equation, or RIME, is a formalism which allows for an elegant and efficient formulation of the physical processes which affect signal propagation, from astrophysical effects to instrumental effects. Its fundamental underlying hypothesis is *linearity*: that transformations along the signal are linear with respect to the basis chosen to represent our signal.

Consider a single quasi-monochromatic point source in the sky. Its signal at a point in time and space can be described by a complex vector \mathbf{e} . We can then represent physical processes which affect this signal’s propagation using *Jones matrices*. In other words:

$$\mathbf{v} = \mathbf{J} \mathbf{e} \tag{2.1}$$

¹(Smirnov 2011b), (Smirnov 2011c) and (Smirnov 2011d)

where \mathbf{v} is the voltage measured by our antenna, \mathbf{J} the Jones matrix describing the *net* propagation effects which affect our source's signal. Note that \mathbf{J} can be written as a series of matrix products, each individual matrix describing a physical phenomenon. They are then called a *Jones chain*, and the resulting \mathbf{J} is often called the *total Jones matrix*.

A visibility is the correlation of voltage from two antennas. In other words,

$$\mathbf{V}_{pq} = 2\mathbf{v}_p(\mathbf{v}_q)^H \quad (2.2)$$

$$\mathbf{V}_{pq} = 2\mathbf{J}_p\mathbf{e}(\mathbf{J}_q\mathbf{e})^H \quad (2.3)$$

$$\mathbf{V}_{pq} = 2\mathbf{J}_p\mathbf{e}\mathbf{e}^H\mathbf{J}_q^H \quad (2.4)$$

where \mathbf{J}_p corresponds to the signal propagation chain of antenna p , and \mathbf{J}_q for antenna q . Note that a factor of 2 has been introduced here, as a matter of convention. This is due to the definition of the Stokes parameter in relation to our \mathbf{e} outer product.

If we choose to use xyz as our coordinates, with z the direction of propagation of our signal, then [Hamaker and Bregman 1996] show that the following relation holds:

$$2\mathbf{e}\mathbf{e}^H = 2 \begin{bmatrix} \langle e_x e_x^* \rangle & \langle e_x e_y^* \rangle \\ \langle e_y e_x^* \rangle & \langle e_y e_y^* \rangle \end{bmatrix} = \begin{bmatrix} I + Q & U + iV \\ U - iV & I - Q \end{bmatrix} = \mathbf{B} \quad (2.5)$$

We can thus write:

$$\mathbf{V}_{pq} = \mathbf{J}_p \mathbf{B} \mathbf{J}_q^H \quad (2.6)$$

This gives us an elegant formulation of the relationship between the signal emitted by an astrophysical source and its corresponding measured visibility. The Stokes parameters of our source can be directly calculated from our measured visibility, provided \mathbf{J}_p and \mathbf{J}_q are known. Of course, in practice, they are not, and must therefore be modelled. To do this, we must expand each Jones matrix into a corresponding Jones chain.

2.2 Expanding our Jones Chain

Having written our RIME as a matrix multiplication problem, we can now begin to differentiate between different types of Jones matrices. \mathbf{J}_p describes the *aggregate* effects which occur over the course of the signal's propagation to our antenna p . It can be split into a Jones chain of n separate matrices, corresponding to different effects:

$$\mathbf{J}_{sp}^H = \prod_1^n \mathbf{J}_{nsp}^H = \mathbf{J}_{1sp}^H \mathbf{J}_{2sp}^H \dots \mathbf{J}_{nsp}^H \quad (2.7)$$

$$\mathbf{J}_{sp} = \mathbf{J}_{nsp} \dots \mathbf{J}_{2sp} \mathbf{J}_{1sp} \quad (2.8)$$

Since the Jones terms are applied sequentially to the brightness matrix, starting with \mathbf{J}_{1sp} , the terms to the right of our decomposition of \mathbf{J}_{sp} can be said to occur 'at the source', i.e. before those to the left (said to occur 'at the antenna').

Our aim is thus to find the Jones chain which most concisely describes the different *types* of effects affecting our signal. In order of increasing complexity, there are three: so-called *geometric* effects, *direction-independent* effects, and *direction-dependent* effects.

2.2.1 Geometric Effects: the Phase Delay Jones Matrix

The physical quantity measured by an interferometric array, the *visibility*, is not a function of the absolute phase of our signal, but rather a function of the *phase difference* between our measured voltages \mathbf{v}_p and \mathbf{v}_q . In other words, it is a function of the phase difference on *baseline* pq , which consists of antennas p and q . The direction which minimises this difference is called the *phase centre*.

We shall use the conventional coordinate system and notations ((Smirnov 2011a), (Thompson et al. 2001), etc). We thus have a z axis pointing towards the phase centre, and an antenna p at coordinates $\mathbf{u}_p = (u_p, v_p, w_p)$. The phase difference between p and phase centre (where, by definition, $\mathbf{u} = 0$) for a signal arriving from direction $\boldsymbol{\sigma}$ is then:

$$\kappa_p = 2\pi i((u_p l + v_p m + w_p(n - 1))) \quad (2.9)$$

where $n = \sqrt{1 - l^2 - m^2}$. Here, l, m, n are the direction cosines² of $\boldsymbol{\sigma}$, and \mathbf{u} is defined in units of wavelength³.

Having done this, we can now introduce a scalar *K-Jones* matrix to represent the effect of this phase delay. Since it is scalar, it will commute with all other Jones matrices [see smirnov 2011]. It can be written as:

$$\mathbf{K}_p = e^{-i\kappa_p} = e^{-2\pi i(u_p l + v_p m + w_p(n - 1))} \quad (2.10)$$

2.2.2 The Coherency Matrix

The commutation property of \mathbf{K}_p with other Jones matrices allow us to always place it at the rightmost end of our Jones chain. We can thus write our Jones chain as follows:

$$\mathbf{J}_p = \mathbf{G}_p \mathbf{K}_p \quad (2.11)$$

$$(2.12)$$

Here, we have decoupled the nominal phase delay term (\mathbf{K}_p) from all ‘corrupting’ effects (\mathbf{G}_p). We can take this one step further by defining the *source coherency*, \mathbf{X}_{pq} , as follows:

$$\mathbf{X}_{pq} = \mathbf{K}_p \mathbf{B}_{pq} \mathbf{K}_p^H \quad (2.13)$$

$$\mathbf{V}_{pq} = \mathbf{G}_p \mathbf{X}_{pq} \mathbf{G}_q^H \quad (2.14)$$

This is useful on a conceptual level: the process of *calibration* is now to find a best estimate for \mathbf{G}_p , which contain all non-‘geometric’ physical effects on the signal’s propagation from an astrophysical source to our voltage measurement.

²The $n - 1$ term in the exponential is due to the fact that, at phase centre, $\kappa_p = 0$ for all \mathbf{u} and $n = \sqrt{1 - 0 - 0} = 1$.

³This means that, for a given baseline pq , \mathbf{u} will vary as a function of frequency.

On a practical level, using the coherency matrix \mathbf{X} allows us to write our RIME more concisely, by absorbing the geometric effects into the core of our RIME. While not strictly necessary, it can be a useful thing to do.

2.3 Multiple Point Sources

So far, \mathbf{B} represents the signal from a single point source. However, the formalism can be extended to multiple point sources fairly easily. This is because electric fields – and therefore radio signals – are additive. If our sky contains s point sources, then our RIME becomes:

$$\mathbf{V}_{pq} = \sum_s \mathbf{J}_{sp} \mathbf{B}_s \mathbf{J}_{sq}^H \quad (2.15)$$

We now expand our Jones chain as before. Some, but not all, elements in the chain will only depend on the antenna. These will be the same for all sources. We can thus write our Jones chain as:

$$\mathbf{J}_{sp} = G_p E_{sp} K_{sp} \quad (2.16)$$

Note that we have kept the source-dependent effects (i.e. E_{sp} those occurring ‘at the source’) are to the right of our chain, and the antenna-dependent (G_p) effects to the left. K_{sp} is a scalar and can thus be moved at will; it is therefore placed at the far right to recover the coherency matrix if necessary.

Our multiple-source RIME can thus be written in the following form:

$$\mathbf{V}_{pq} = G_p \left(\sum_s \mathbf{E}_{sp} \mathbf{K}_{sp} \mathbf{B}_s \mathbf{K}_{sq}^H \mathbf{E}_{sq}^H \right) G_q^H \quad (2.17)$$

This ‘onion’ form of the RIME is usually sufficient to describe signal propagation in radio-interferometric arrays. We find the three types of Jones matrices promised earlier: the geometric effects accounted for by \mathbf{K} , the direction-dependent effects modeled into \mathbf{E} , and the direction-independent effects (antenna-based effects) modeled into \mathbf{G} .

There are still limitations to this RIME; notably, it assumes that the sky consists entirely of point sources (absence of diffuse emission), and that Jones matrices are time-independent. These are of course unphysical hypotheses, though they are a very good first approximation. We shall now address these two points.

2.4 Diffuse Emission: the Full-sky RIME

2.4.1 Deriving the Fully-Sky RIME

If we want to be able to take diffuse emission properly into account, we must go from our set of discrete point sources \mathbf{B}_s and integrate the underlying continuous brightness distribution $\mathbf{B}(\sigma)$ over all possible directions. This gives us the following expression:

$$\mathbf{V}_{pq} = \int_{4\pi} \mathbf{J}_p(\sigma) \mathbf{B}(\sigma) \mathbf{J}_q^H(\sigma) d\Omega \quad (2.18)$$

Here, effects such as our radio beam lie in the Jones matrices. By performing the analysis of [thompson 2001, sect 3.1], we can rewrite this expression in terms of a sine projection of the sphere onto the (l, m) plane tangential at field centre. The integral then becomes:

$$\mathbf{V}_{pq} = \int_{l,m} \mathbf{J}_p(\boldsymbol{\sigma}) \mathbf{B}(\boldsymbol{\sigma}) \mathbf{J}_q^H(\boldsymbol{\sigma}) \frac{dldm}{n} \quad (2.19)$$

Having written this, and using \mathbf{l} as shorthand (l, m) , we can once again decompose our Jones matrix into a Jones chain containing a direction-independent term \mathbf{G} , a direction-dependent term \mathbf{E} , and the phase term \mathbf{K} . Substituting this into our integral, we get the following expression:

$$\mathbf{V}_{pq} = \mathbf{G}_p \left(\int_{\mathbf{l}} \frac{1}{n} \mathbf{E}_p(\mathbf{l}) \mathbf{B} \mathbf{E}_q(\mathbf{l}) \mathbf{K}_p(\mathbf{l}) \mathbf{K}_q^H(\mathbf{l}) dldm \right) \mathbf{G}_q^H \quad (2.20)$$

$$= \mathbf{G}_p \left(\int_{\mathbf{l}} \frac{1}{n} \mathbf{E}_p(\mathbf{l}) \mathbf{B} \mathbf{E}_q(\mathbf{l}) e^{-2\pi i (u_{pq}l + v_{pq}m + w_{pq}(n-1))} dldm \right) \mathbf{G}_q^H \quad (2.21)$$

where

$$u_{pq} = u_p - u_q \quad v_{pq} = v_p - v_q \quad w_{pq} = w_p - w_q \quad (2.22)$$

This is a three-dimensional Fourier transform. It can be reduced to a two-dimensional Fourier transform by writing the n -dependence in the exponential (and normalisation) as a Jones matrix, thus removing the *non-coplanarity* terms from the explicit RIME. We can thus define the following:

$$\mathbf{W}_p = \frac{1}{\sqrt{n}} e^{-2\pi i w_p(n-1)} \quad (2.23)$$

$$B_{pq} = \mathbf{E}_p \mathbf{W}_p \mathbf{B} \mathbf{W}_q^H \mathbf{E}_q^h \quad (2.24)$$

and write our RIME in its final form:

$$\mathbf{V}_{pq} = \mathbf{G}_p \left(\int_{\mathbf{l}} \mathbf{B}_{pq}(\mathbf{l}) e^{-2\pi i (u_{pq}l + v_{pq}m + w_{pq}(n-1))} dldm \right) \mathbf{G}_q^H \quad (2.25)$$

Note that \mathbf{B} was the actual sky brightness distribution as a function of direction, but now \mathbf{B}_{pq} is the sky brightness *as seen by baseline pq* - there is no *a priori* reason this should be the same for all baselines.

2.4.2 Recovering the van Cittert-Zernike Theorem

Earlier calibration models and algorithm rely on the hypothesis that all baselines see the same sky. This is the *fundamental premise of self-calibration*. The topic of self-cal will be covered in Section 1.5.1. This premise only holds when all Direction-Dependent Effects (henceforth referred to as DDEs) are identical for all baselines (and therefore for all antennas). This is a necessary condition for the apparent sky \mathbf{B}_{pq} to be the same for all baselines⁴, as it allows us to write:

$$\mathbf{E}_p(\mathbf{l}) \mathbf{W}_p(\mathbf{l}) = \mathbf{E}(\mathbf{l}) \mathbf{W}(\mathbf{l}) \quad (2.26)$$

⁴ \mathbf{B}_{pq} would then correspond to the ‘true’ sky attenuated by the power beam, in the traditional view

$$\mathbf{B}_{pq}(\mathbf{l}) = \mathbf{B}_{app}(\mathbf{l}) = \mathbf{E}(\mathbf{l}) \mathbf{W}(\mathbf{l}) \mathbf{B}(\mathbf{l}) \mathbf{W}^H(\mathbf{l}) \mathbf{E}^H(\mathbf{l}) \quad (2.27)$$

If this condition is met, we can then rewrite the full-sky RIME as:

$$\mathbf{V}_{pq} = \mathbf{G}_p \mathbf{X}_{pq} \mathbf{G}_q^H \quad (2.28)$$

where $\mathbf{X}_{pq} = \mathbf{X}(u_{pq}, v_{pq}) = \mathbf{X}(\mathbf{u})$. Comparing Eqs. (2.13) and (2.25) directly shows that the coherency matrix is simply the two-dimensional Fourier transform of $\mathbf{B}_{app}(\mathbf{l})$. We can thus call $\mathbf{X}(\mathbf{u})$ the *sky coherency*, in keeping with our nomenclature for the RIME of a point source.

Note that deriving the van Cittert-Zernike theorem ((van Cittert 1934), covered in (Thompson et al. 2001)) from the RIME was simply of matter of treating phase as a Jones matrix in its own right⁵. A significant consequence of this is that DDEs can be incorporated within the RIME formalism.

2.5 Time-dependent Jones matrices, Smearing, and Decoherence

2.5.1 Time-dependence of Jones matrices

Until this point, we have not considered any kind of time variability. In effect, Eq. (2.28) describes the snapshot taken by an interferometer for a single measurement. Limiting ourselves to this scenario, however, constrains the sampling of the uv -plane which can be performed. Indeed, interferometers generally rely on the Earth's rotation to rotate their baselines pq , thus increasing uv -coverage at no additional cost. For Eq. (2.28) to hold throughout an observation, we must therefore assume that B_{app} remains constant in time over the course of the observation. In effect, this means assuming that

$$\mathbf{E}_p(t, \mathbf{l}) = \mathbf{E}_p(\mathbf{l}) = \mathbf{E}(\mathbf{l}) \quad \forall (t, p) \quad (2.29)$$

The above means that direction-dependent effects must be time-independent for Eq. (2.28) to hold. We can thus split direction-dependent effects into two categories: *trivial* DDEs, which satisfy this condition (and can thus be solved for within the RIME formalism), and *non-trivial* DDEs, which are - as the name indicates - non-trivial to account for within the RIME formalism. An example of a trivial DDE is the primary gain; and example of a non-trivial (i.e. time-variable) DDE is ionospheric turbulence.

2.5.2 Smearing and Decoherence

Of course, our Jones matrices are not the only time-dependent part of the RIME formalism. To image with interferometric arrays, radio astronomers rely on the Earth's rotation to better sample uv -space, a technique referred to as *super-synthesis* (Joardar et al. (2010)⁶). This means that \mathbf{u} becomes a *time-dependent* variable.

⁵Noordm, J.E. 1996, AIPS++, Note 185: The Measurement Equation of a Generic Radio Telescope

⁶(link to paper)

Furthermore, if we choose to define \mathbf{u} in terms of wavelength, \mathbf{u}_p becomes dependent in frequency. Our time-independent, frequency-independent RIME thus becomes only valid for infinitesimal increments in time and frequency.

In practice, measurements made by any interferometric array is actually averaged over the integration time of the measurement, as well as the frequency channel size. A better formulation is therefore to explicitly write the RIME as an integration over time and frequency bins:

$$\langle \mathbf{V}_{pw} \rangle = \frac{1}{\Delta t \Delta \nu} \int_{t_0}^{t_1} \int_{\nu_0}^{\nu_1} \mathbf{V}_{pq}(t, \nu) dv dt \quad (2.30)$$

$$= \frac{1}{\Delta t \Delta \nu} \int_{t_0}^{t_1} \int_{\nu_0}^{\nu_1} \mathbf{J}_p(t, \nu) \mathbf{B} \mathbf{J}_q^H(t, \nu) \quad (2.31)$$

$\mathbf{J}(t, \nu)$ describes the propagation of an electromagnetic signal through various physical processes. This signal has a complex phase, which is variable in both time and frequency. Since it is a rotating vector, integrating over any time or frequency band will always result in a *net loss* in amplitude in the measured $\langle \mathbf{V} \rangle$. This mechanism is commonly referred to as *time/bandwidth width decorrelation* or *smearing* (Smirnov (2011a)).

The general effect is referred to as *decoherence*, and the specific case of decoherence caused by the \mathbf{K} term is referred to as *smearing*.

Smearing increases with baseline length (\mathbf{u}_{pq}) and distance from phase centre ((l, m)). The noise amplitude, however, does not decrease. This means that smearing results in a decrease in sensitivity, which becomes significant when attempting to do wide-field, high-resolution images (see section [PLUG GROTH WORK SHAMELESSLY]).

In the context of the RIME, smearing is an element-by-element operation, i.e. different elements do not affect each other. Treating smearing within the RIME is thus a trivial expansion of the scalar equations.

Assuming that Δt and $\Delta \nu$ are small enough that the amplitude of \mathbf{V}_{pq} remains constant over the integration band (i.e. that \mathbf{V}_{pq} is well-sampled by our instrument), then a useful first-order approximation is:

$$\langle \mathbf{V}_{pw} \rangle \simeq \text{sinc} \frac{\Delta \Psi}{2} \text{ sinc} \frac{\Delta \Phi}{2} \mathbf{V}_{pq}(t_{mid}, \nu_{mid}) \quad (2.32)$$

where

$$t_{mid} = (t_0 + t_1)/2 \quad (2.33)$$

$$\nu_{mid} = (\nu_0 + \nu_1)/2 \quad (2.34)$$

$$\Delta \Psi = \arg \mathbf{V}_{pq}(t_1, \nu_{mid}) - \arg \mathbf{V}_{pq}(t_0, \nu_{mid}) \quad (2.35)$$

$$\Delta \Phi = \arg \mathbf{V}_{pq}(t_{mid}, \nu_1) - \arg \mathbf{V}_{pq}(t_{mid}, \nu_0) \quad (2.36)$$

This equation is convenient to determine the impact of decorrelation for a source at a given distance from phase centre. Note, however, that it can only - by definition - be valid for a single source at a time. If using a RIME such as Eq. (2.17), then it can be calculated for each source individually.

2.6 Noise

The RIME presented thus far has been for an ideal case, free of noise in our measured visibility. In practice, each complex visibility will be affected by uncorrelated Gaussian noise⁷, which means that a RIME of the same form as Eq. (2.17) would have to be formulated at follows:

$$\mathbf{V}_{pq} = \mathbf{G}_p \left(\sum_s \mathbf{E}_{sp} \mathbf{K}_{sp} \mathbf{B}_s \mathbf{K}_{sq}^H \mathbf{E}_{sq}^H \right) \mathbf{G}_q + \sigma_{pq} \quad (2.37)$$

where σ_{pq} is a $(2, 2)$ matrix with real and complex parts in each component. A similar addition can be made for any of the RIMEs presented here.

This noise sets a hard limit on the sensitivity achieved for a given observation, and ‘reaching the noise’ becomes the gold standard of calibration ((Smirnov 2011b)). One must then take σ_{pq} into account properly when solving for the Jones matrices.

⁷Detailed treatment given in (Thompson et al. 2001), section 6.2

Chapter 3

Analysing the Variance of Gain Solutions

3.1 Foreword

This section covers published work on an interferometric algorithm, along with its underlying theoretical framework. Bla bla

3.2 Introduction

Interferometers sample Fourier modes of the sky brightness distribution corrupted by instrumental and atmospheric effects rather than measuring the sky brightness directly. This introduces two problems for astronomers to invert: calibration and imaging. Both of these problems are ill-conditioned.

The problem of imaging consists of correcting for the incomplete uv -coverage of any given interferometer by deconvolving the instrument's Point-Spread Function (PSF) from images. Its poor conditioning comes from our limited a priori knowledge of the sky brightness distribution, combined with large gaps in our uv -coverage, which prevents us from placing strong constraints on image deconvolution. It can be better-conditioned in different ways, including through the use of weighting schemes (see Briggs 1995; Yatawatta 2014, and references therein) to improve image fidelity at the start of deconvolution. When inverting the imaging problem, we often assume that the sky is stable within the domain (i.e. is constant in time and frequency). There are exceptions, such as wide-band deconvolution algorithms (e.g. Rau & Cornwell 2011) that explicitly take into account the sky's frequency-dependence, but still assume that the sky brightness distribution does not vary with time.

The problem of calibration is what concerns us in this paper. It consists of estimating and correcting for instrumental errors (which includes effects such as antenna pointing errors, but also the phase-delays caused by ionospheric activity, troposphere, etc). Calibration consists of solving for gain estimates, where a gain models the relationship between the electromagnetic field of an astrophysical source and the voltage that an antenna measures for this source. Because measurements are noisy, calibration

often involves some fine-tuning of solution intervals, to ensure that the solutions are well-constrained while the solution intervals stay as small as signal-to-noise allows. The calibration inverse problem involves three competing statistical effects: thermal noise in the measurements, true gain variability, and sky model incompleteness. If gain solutions are sought individually for each measurement, then calibration estimates will be dominated by thermal noise, and will not adequately describe the actual gains. Similarly, if a single gain estimate is fitted to too many measurements, the intrinsic gain variability will be “averaged out”; for example, a choice of time and frequency interval that is too large will cause the solver to estimate a constant gain while the underlying function varies quickly, thereby missing much of the gain structure. This will introduce error which will be correlated in time and frequency. This occurs, for example, when solving for ionospheric phase delays: in the most extreme case, where the solution interval is significantly larger than the scale of ionospheric fluctuations, its varying phase can average out to zero over the interval in time and frequency. Finally, if the model being fitted is incomplete, unmodeled physical flux will likely be absorbed unpredictably into both the gain solutions and the residual visibilities: this absorption of physical flux into gain solutions is known as source suppression (see Grobler et al. 2014; Kazemi & Yatawatta 2013, and references therein).

In practice, it is reasonable to assume that gain variation is generally slower than some given scale: we can then reduce the noise of our gain estimates by finding a single gain solution for a small number of measurements, assuming that the underlying gain variation is very small and stable over short intervals. This is *generally* a valid hypothesis, but the specific value for the variation scale can be contentious. Indeed, while the noise level can often be treated as constant throughout an observation, the gain variability itself is generally not constant: there will be time periods where the gains will tend to remain constant for longer, and others where variability will be very quick. This means that, for any choice of calibration interval, some gain estimates will be better than others, and almost all could have been improved (at a cost to others) by a different choice of time (and frequency) intervals.

Since we have measurements which are better-calibrated than others (in that better estimates for their gains were obtained through chance alone), we could, in principle, take inspiration from “lucky imaging” (an optical-domain method for making good images: for more details, see Fried 1978, and references therein) to weigh our visibilities according to their calibration quality. Those weights would in effect be an improvement of currently existing methods such as clipping noisy residual visibilities: in the extreme case where all visibilities are equally-well calibrated except a few which are extremely noisy, it should be equivalent to clipping. Otherwise, the weights should show at least a slight improvement over clipping.

The key finding of the present paper is a fundamental relationship between the covariance matrices of residual visibilities and the map of the covariance in the image-plane: the “Cov-Cov relationship” between visibility covariance to image-plane covariance. We show that the pixel statistics in the image-plane are determined by a “noise-PSF”, convolved with each source in the sky (modeled or not). This noise-PSF is the product of the Fourier transforms of the gain covariance matrix with each cell mapped not from uv

space to lm coordinates but rather between their respective covariance spaces - from a new differential Fourier plane (henceforth “ $(\delta u \delta v)$ -plane) to the image-plane covariance space $\delta l \delta m$. This image-plane covariance space describes the variance in each pixel and the covariance between pixels¹. It describes the expected calibration artefacts and thermal noise around each source, does not vary as a function of direction, and is convolved with each source in the field to yield the final error map. Because all unwanted (in our case, unphysical) signal can be thought of as noise, we will refer to the pixel variance map as the “noise-map”.

The notion of a $(\delta u \delta v)$ -plane arises organically from the framework of radio interferometry: we are associating a *correlation* between visibilities to *coordinates* in covariance space, just as we associate the visibilities themselves to the uv -domain. The $(\delta u \delta v)$ -plane is the natural domain of these correlations. As previously stated, even if all sources in the field are perfectly known and modeled, a poor choice of calibration interval can introduce correlated noise in the residuals, which would then introduce larger variance near sources in the noise-map. Conversely, if calibration is perfect, the noise-map should be completely flat (i.e. same variance for all pixels), as there would be no noise-correlation between pixels.

The main result of this paper consists of describing a new adaptive, quality-based weighting scheme based on this insight. Using the Cov-Cov relationship, we can create a new weighting scheme by estimating the residual visibility covariance matrix in a given observation. By weighting visibilities so as to change their covariance matrix, one can change the shape of the noise-PSF and thus improve the final image: this manifests as either decreased noise or decreased calibration artefacts. Note that this weighting is applied after calibration, but before image deconvolution: applying it will therefore not only improve the residual noise in the image, and thus the sensitivity achievable with a given pipeline, but will also improve deconvolution by minimising calibration artefacts in the field: it should thus effectively remove spurious, unphysical emission from final data products. Estimating the covariance matrix is the main difficulty of our framework: we do not know the underlying covariance matrix, and the conditioning of our estimation thereof is limited by the number of measurements within each solution interval. As such, we have no guarantee that our estimate of the corrected visibility covariance matrix is accurate. This problem can be alleviated, for example by estimating the covariance matrix for the antenna gains themselves, and use it to build the visibility covariance matrix: this effectively improves conditioning (cf Sec. 3.5).

This paper is split into four main sections. In Section 3.3, we derive the Cov-Cov relationship. With its newfound insights, we propose quality-based weighting schemes with which to improve radio interferometric images in Section 3.4. We follow in Section 3.5 by showing how to estimate, from real data, the covariance matrix from which the quality-based weights are derived. Our approach seems to give good results. Finally, we close the paper on a discussion of the applicability and limitations of the quality-based weighting scheme.

¹The noise-PSF also relates δw to δn , as shown in the matrix formalism, but this is not explicitly referenced in the text since visibility space is usually referred to as “the UV-plane” in literature, rather than “the UVW-space”.

<u>Scalars</u>	
n_{pix}	Total number of pixels in image-plane & number of cells in uv -grid
n_{ant}	Total number of antennas in the array
n_b	Number of visibilities
b	Index for a single visibility.
	Equivalent to $(pq, t\nu)$
τ	Equivalent to (t, ν)
<u>Vectors</u>	
$\tilde{\mathbf{y}}$	Residual image vector, size n_{pix}
ϵ	Vector of ϵ , size n_{pix}
$\tilde{\boldsymbol{\gamma}}$	Contains gain products, size n_b . See Eq. 3.12
$\mathbf{1}$	Vector containing 1 in every cell, size n_b
$\delta\mathbf{u}_{bb'}$	Vector of coordinates in differential Fourier plane, of length 3.
\mathbf{l}_d	Vector of sky coordinates, of length 3.
<u>Matrices</u>	
$\mathbf{V}_{pq}^{t\nu}$	Visibility seen by a baseline pq at time and frequency t, ν . Size 2×2 .
$\mathbf{K}_{p,t\nu}^d$	Fourier kernel for direction d , antenna p and one (t, ν) pair. Size 2×2 .
$\mathbf{J}_{p,t\nu}$	Jones matrix for antenna p for one (t, ν) pair. Contains the gains information. Size 2×2
\mathbf{B}	Sky brightness distribution matrix, of size 2×2 .
\mathbf{N}	Noise matrix, of size 2×2 . Contains a single realisation n of the thermal noise in each cell.
\mathcal{F}	Fourier transform matrix, of size $n_{\text{pix}} \times n_{\text{pix}}$.
\mathcal{S}_b	Baseline selection matrix, which picks out 1 visibility out of the full set. Size $n_{\text{pix}} \times n_b$
\mathcal{C}_b	$n_{\text{pix}} \times n_{\text{pix}}$ convolution kernel that defines the PSF.
$\mathcal{F}_{bb'}$	Convolution matrix mapping one $\delta u \delta v$ to $\delta l \delta m$. The set of all $\mathcal{F}_{bb'}$ determines the noise-PSF. Size $n_{\text{pix}} \times n_{\text{pix}}$.

Table 3.1. Table recapitulating the meaning and dimensions of vectors and matrices used in Sec. 3.3.1. Only scalars which give matrix dimensions or indices are given here.

3.3 Building the Noise Map

In this section, we derive our first fundamental result: the Cov-Cov relationship, Eq. 3.25, which describes how the statistics of residual visibilities (and thus the antenna calibration solutions, henceforth “gains”) relate to the statistics of the image plane, i.e. of images made using the associated visibilities. The dimensions of the matrices (denoted by boldface capital letters) and vectors (denoted by boldface lowercase letters) used in this paper are given in Table 3.1, along with the scalar numbers used to denote specific dimensions. All other variables are scalars.

3.3.1 The Cov-Cov Relationship in the $\delta u \delta v$ plane

Let us begin by defining visibility gains. Using the Radio Interferometry Measurement Equation formalism for a sky consisting of a single point source (Hamaker et al. (1996), Smirnov (2011a), and companion papers), we can write the following relation between the sky and the signal as measured by a single baseline at time t and frequency ν :

$$\mathbf{V}_{pq}^{t\nu} = \sum_d \mathbf{K}_{p,t\nu}^d \mathbf{J}_{p,t\nu}^d \mathbf{B}_\nu^d (\mathbf{J}_{q,t\nu}^d)^H (\mathbf{K}_{q,t\nu}^d)^H + \mathbf{N} \quad (3.1)$$

All the quantities above are 2×2 matrices. Eq. 3.1, implies a linear relationship between the coherency matrix \mathbf{B}_ν^d and the visibilities recorded by a given baseline ($\mathbf{V}_{pq}^{t\nu}$), with the addition of a thermal noise matrix \mathbf{N} , which is also of shape 2×2 and contains different complex-valued realisations of the noise in each cell. Since electric fields are additive, the sky coherency matrix can be described as the sum of the contributions from individual sources in directions d in the sky. We also assume that the sky does not vary over time, i.e. that \mathbf{B}_ν^d is not a function of time. The Jones matrices ($\mathbf{J}_{...,t\nu}^d$) contain the antenna gain information in matrix form, while $\mathbf{K}_{...,t\nu}^d$ is the Fourier kernel. Let us limit ourselves to the scalar case, which corresponds to assuming that emission is unpolarised. We assume that $\mathbf{B}^d = s_d \mathbf{I}$, where s is the flux of our single point source and \mathbf{I} is the 2×2 identity matrix. We also assume that $\mathbf{J}_{p,t\nu} = g_{p,t\nu} \mathbf{I}$, where $g_{p,t\nu}^{t\nu}$ is the complex-valued gains of antenna p at time t and frequency ν . This means that we assume that the gains are direction-independent, and so $\mathbf{J}_{...,t\nu}^d$ becomes $\mathbf{J}_{...,t\nu}$. Similarly, $\mathbf{K}_{p,t\nu}^d = k_{p,t\nu}^d \mathbf{I}$, the Fourier kernel in the direction of the source, d . \mathbf{N} has 1 realisation of ϵ in each cell, where:

$$\epsilon \sim \mathcal{N}(0, \sigma) + i\mathcal{N}(0, \sigma) \quad (3.2)$$

where σ is the variance of the thermal noise. Let us denote each (t, ν) pair by τ , and ignore the sky’s frequency-dependence. The following scalar formulation is then equivalent to Eq. 3.1:

$$V_{pq}^\tau = \left(\sum_d s_d k_{p,\tau}^d \overline{k_{q,\tau}^d} \right) g_p^\tau \overline{g_q^\tau} + \epsilon \quad (3.3)$$

$$k_{p,\tau}^d = \exp(2\pi i (u_{p,\tau} l_d + v_{p,\tau} m_d + w_{p,\tau} (n_p - 1))) \quad (3.4)$$

Calibration is the process of finding an accurate estimate of \hat{g}_p^τ for all antennas p , at all times t and frequencies ν . Since we are in a direction-independent regime, the quality of our calibration then determines the statistical properties of the residual visibilities (and the image-plane equivalent, the residual image). The residual visibilities associated with calibration solutions are defined as our measured visibilities minus the gain-corrupted model visibilities. \hat{g}_p^τ then denotes our calibration estimate for g_p^τ . We now begin to limit the generality of our framework by assuming that all sufficiently bright sources have been modeled and subtracted: unmodeled flux is then negligible. We can then write the residual visibilities as:

$$\tilde{r}_{pq}^\tau = \sum_d s_d \left(k_{p,\tau}^d \overline{k_{q,\tau}^d} \right) \left(g_p^\tau \overline{g_q^\tau} - \hat{g}_p^\tau \overline{\hat{g}_q^\tau} \right) + \epsilon \quad (3.5)$$

The flux values in the image-plane pixels² are the Fourier transform of the visibility values mapped onto each pixel. This can be written as follows:

$$\tilde{\mathbf{y}} = \begin{pmatrix} \vdots \\ \sum_{pq} I_{pq,lm}^r \\ \vdots \end{pmatrix} \quad (3.6)$$

$$I_{pq,lm}^r = \sum_\tau \omega_{pq,\tau} \tilde{r}_{pq}^\tau k_{pq,\tau}^{lm} \quad (3.7)$$

where lm are the directional cosine positions of a given pixel, and $k_{pq,\tau}^{lm} = k_{p,\tau}^d \overline{k_{q,\tau}^d}$ the Fourier coefficient mapping a point in Fourier space to a point on the image-plane. $\omega_{pq,\tau}$ is the weight associated to a given visibility.

Let us now write this using a matrix formalism. The contribution of a single visibility $b = (pq, \tau)$ to the image-plane residuals can be written as:

$$\tilde{\mathbf{y}}_b = \mathcal{F}^H \mathbf{S}_b \omega_b (\kappa_b \tilde{\gamma} + \epsilon) \quad (3.8)$$

$$\tilde{\mathbf{y}} = \sum_b \tilde{\mathbf{y}}_b \quad (3.9)$$

where ϵ is a vector of the ϵ of Eq. 3.2 and $\tilde{\mathbf{y}}$ is a vector of size n_{pix} , with

$$\kappa_b = \sum_d s_d \kappa_b^d \quad (3.10)$$

$$\kappa_b^d = k_{p,\tau}^d \overline{k_{q,\tau}^d} = k_{pq,\tau}^{lm} \quad (3.11)$$

$$\tilde{\gamma}_b = g_p^\tau \overline{g_q^\tau} - \hat{g}_p^\tau \overline{\hat{g}_q^\tau} \quad (3.12)$$

$$\tilde{\gamma} = \begin{pmatrix} \vdots \\ \tilde{\gamma}_b \\ \vdots \end{pmatrix} \quad (3.13)$$

and w_b is the scalar weight associated with each visibility. By default, $w_b = \frac{1}{n_b}$: all visibilities then have the same weight, and $\tilde{\mathbf{y}}$ then becomes the average of all $\tilde{\mathbf{y}}_b$. $\tilde{\gamma}$ is a vector of all $\tilde{\gamma}_b$, and thus of size n_b . \mathcal{F} is the Fourier kernel, of size $n_{\text{pix}} \times n_{\text{pix}}$. \mathbf{S}_b is a matrix of size $n_{\text{pix}} \times n_b$: its purpose is to encode the uv -coverage. Each \mathbf{S}_b contains only a single non-zero cell, different for different \mathbf{S}_b . The height (number of rows) of \mathbf{S}_b is determined the size of the uv -grid, and its length (number of columns) by the number of visibilities.

²As opposed to the Fourier-plane pixels, which are the elements of the grid onto which the measured visibilities are mapped for imaging.

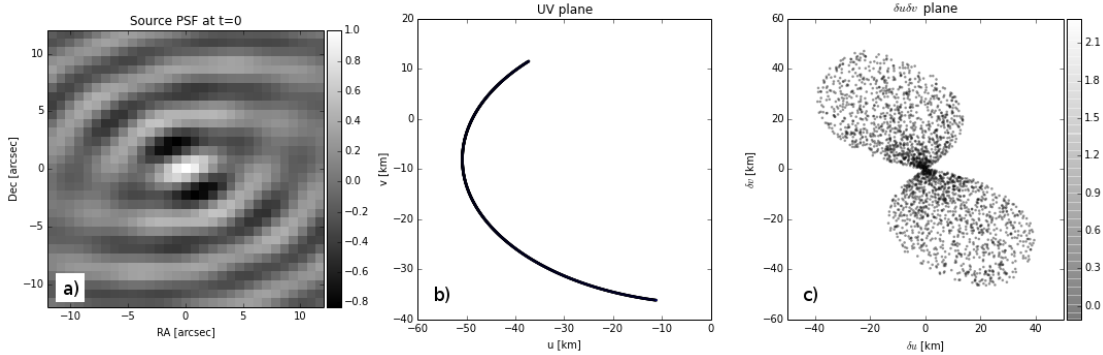


Figure 3.1. Fig. 3.1a shows the PSF image of a simulated 1Jy source at phase centre. Colourbar units are in Jansky. Fig. 3.1b shows the associated UV track, and Fig. 3.1c the corresponding $(\delta u, \delta v)$ tracks. Note that the $\delta u \delta v$ plane does not have a homogeneous point density, but is denser near its origin: here, this is shown by plotting only 1 random point in 10000.

The order of operations is thus: each residual visibility ($\kappa_b \tilde{\gamma} + \mathbf{n}$) is assigned some weight w_b and its uv -coordinates are set by \mathcal{S}_b . The inverse Fourier transform (\mathcal{F}^H) is then applied to this grid, and so we recover its image-plane fringe. By averaging over all fringes, we recover the dirty image.

The residual image will thus depend on three quantities: the residual gains, the flux in the image, and the weighting scheme. Let us consider the relationship between the statistics of residual visibilities and the variance at a given point in the corresponding residual image.

3.3.2 Statistical Analysis

In the following analysis, we treat our gain solutions and thermal noise as random variables in order to compute the covariance matrix of our residual image, $\text{Cov}\{\tilde{\mathbf{y}}\}$. The diagonal of this matrix gives the variance for each pixel, while the wings give the covariance between pixels. Using the property that $\text{Cov}\{\mathbf{Ax}\} = \mathbf{A}\text{Cov}\{\mathbf{x}\}\mathbf{A}^H$, we can apply the $\text{Cov}\{\cdot\}$ operator to Eq. 3.9 to write:

$$\text{Cov}\{\tilde{\mathbf{y}}\} = \sum_{bb'} \underbrace{\mathcal{F}^H w_b w_{b'} \kappa_b \overline{\kappa_{b'}}}_{\stackrel{\text{def}}{=} \phi_{bb'}} \mathcal{S}_b \text{Cov}\{\tilde{\gamma}\} \mathcal{S}_{b'}^T \mathcal{F} \quad (3.14)$$

$$+ \sum_b w_b^2 \sigma^2 \underbrace{\mathcal{F}^H \mathcal{S}_b \mathbf{I} \mathcal{S}_b^T \mathcal{F}}_{\stackrel{\text{def}}{=} \mathcal{C}_b} \quad (3.15)$$

$$= \sum_{bb'} \phi_{bb'} \mathcal{F}^H \mathcal{S}_b \text{Cov}\{\tilde{\gamma}\} \mathcal{S}_{b'}^T \mathcal{F} + \sum_b w_b^2 \sigma^2 \mathcal{C}_b \quad (3.16)$$

So far, we have only applied definitions. The net effect of $\mathcal{S}_b \text{Cov}\{\tilde{\gamma}\} \mathcal{S}_{b'}^T$ (dimensions of $n_{\text{pix}} \times n_{\text{pix}}$) is to encode where a given baseline samples the uv -plane, and map *one* cell at matrix coordinates (b, b') from the correlation matrix $\text{Cov}\{\tilde{\gamma}\}$ onto the visibility grid. \mathcal{S}_b is not the gridding kernel, but rather the sampling matrix, which determines where we have measurements and where we do not. We can thus write that $\mathcal{S}_b \text{Cov}\{\tilde{\gamma}\} \mathcal{S}_{b'}^T =$

$[\text{Cov}\{\tilde{\gamma}\}]_{bb'} \mathbf{S}_b \mathbf{1} \mathbf{1}^T \mathbf{S}_{b'}^T$, where $[\text{Cov}\{\tilde{\gamma}\}]_{bb'}$ is the value from the appropriate cell and $\mathbf{1}$ is the vector-of-ones of appropriate length (here, n_b). This allows us to write:

$$\text{Cov}\{\tilde{\mathbf{y}}\} = \sum_{bb'} \phi_{bb'} [\text{Cov}\{\tilde{\gamma}\}]_{bb'} \mathcal{F}_{bb'} + \sum_b w_b^2 \sigma^2 \mathcal{C}_b \quad (3.17)$$

$$\text{with } \mathcal{F}_{bb'} = (\mathcal{F}_b)^H \underbrace{\mathcal{F}_{b'}}_{\stackrel{\text{def}}{=} \mathbf{1}^T \mathbf{S}_{b'}^T \mathcal{F}} \quad (3.18)$$

Here, \mathcal{C}_b is a Toeplitz matrix, i.e. a convolution matrix, associated with baseline b . The set of all \mathcal{C}_b defines the convolution kernel which characterises the Point-Spread Function (henceforth PSF) associated with a given uv-coverage, of size $n_{\text{pix}} \times n_{\text{pix}}$. $\mathcal{F}_{bb'}$, meanwhile, is not generally Toeplitz. Its cells can be written as:

$$\mathcal{F}_{bb'}[d, d'] = e^{2i\pi(u_b l_d - u_{b'} l_{d'} + v_b m_d - v_{b'} m_{d'} + (n_d - 1)w_b - (n_{d'} - 1)w_{b'})} \quad (3.19)$$

Let us investigate how the sky brightness distribution (i.e. d -dependence) affects the noise-map. We can write the sum over bb' as two sums: one over $b, b' = b$ and one over $b, b' \neq b$. Thus:

$$\begin{aligned} \text{Cov}\{\tilde{\mathbf{y}}\} &= \sum_b (\phi_{bb} [\text{Cov}\{\tilde{\gamma}\}]_{bb} + w_b^2 \sigma^2) \mathcal{C}_b \\ &\quad + \sum_{b, b' \neq b} \phi_{bb'} [\text{Cov}\{\tilde{\gamma}\}]_{bb'} \mathcal{F}_{bb'} \end{aligned} \quad (3.20)$$

Note that the only direction-dependent terms in the above are s_d and κ_b^d , which are both inside $\phi_{bb'}$ (for both $b = b'$ and $b \neq b'$). By making the approximation that the Fourier kernels of different sources are orthogonal (i.e. that $\kappa_b^d \kappa_{b'}^{d'} = (\kappa_b^d)^2 \delta_{bb'}$)³ we can write:

$$\phi_{bb'} = w_b w_{b'} \kappa_b \overline{\kappa_{b'}} \quad (3.21)$$

$$= w_b w_{b'} \left(\sum_d s_d \kappa_b^d \right) \left(\sum_{d'} s_{d'} \overline{\kappa_{b'}^{d'}} \right) \quad (3.22)$$

$$\approx \sum_d w_b w_{b'} s_d^2 \kappa_b^d \overline{\kappa_{b'}^{d'}} \quad (3.23)$$

$$\phi_{bb'} \approx \sum_d \phi_{bb'}^d \quad (3.24)$$

Note that $\mathcal{F}_{bb} = \mathcal{C}_b$, since those are the coordinates along the diagonal: for these values, the matrix-of-ones at the centre of $\mathcal{F}_{bb'}$ becomes the identity matrix. Note also that $\phi_{bb}^d = w_b^2 s_d^2$, since $\kappa_b^d \overline{\kappa_b^d} = 1$. We can then write Eq. 3.20 as:

$$\begin{aligned} \text{Cov}\{\tilde{\mathbf{y}}\} &= \sum_d \left(\sum_b \phi_{bb}^d \left([\text{Cov}\{\tilde{\gamma}\}]_{bb} + \frac{w_b^2 \sigma^2}{\phi_{bb}} \right) \mathcal{C}_b \right. \\ &\quad \left. + \sum_{b, b' \neq b} \phi_{bb'}^d [\text{Cov}\{\tilde{\gamma}\}]_{bb'} \mathcal{F}_{bb'} \right) \end{aligned} \quad (3.25)$$

where we have now limited our formalism to the case where the sky is dominated by distant point-like sources.

³This hypothesis is equivalent to assuming that the sky is dominated by distant point sources, where “distant” means that the sources are multiple PSF Full-Width Half-Maximum apart

This is our fundamental result: assuming unpolarised emission coming from distant point sources and normally-distributed thermal noise, it gives a direct relationship between the covariance of the residual visibilities and the covariance of the residual image-pixel values. We thus call it the Cov-Cov relationship. It describes the statistical properties of the image-plane as the result of a convolution process changing an average noise level at different points in the image-plane, allowing us to describe the behaviour of variance and covariance in the image. Let us focus on the first

By applying the $\text{Diag}\{\}$ operator (which returns the diagonal of an input matrix as a vector) to both sides of Eq.3.25, we can find an expression for the variance map in the image-plane:

$$\text{Var}\{\tilde{\mathbf{y}}\} = \text{Diag}\{\text{Cov}\{\tilde{\mathbf{y}}\}\} \quad (3.26)$$

$$\begin{aligned} &= \sum_d \left(\sum_b (\phi_{bb}^d [\text{Cov}\{\tilde{\gamma}\}]_{bb} + w_b^2 \sigma^2) \underbrace{\text{Diag}\{\mathcal{C}_b\}}_{=\mathbf{1}} \right. \\ &\quad \left. + \sum_{b,b' \neq b} \phi_{bb'}^d [\text{Cov}\{\tilde{\gamma}\}]_{bb'} \text{Diag}\{\mathcal{F}_{bb'}\} \right) \end{aligned} \quad (3.27)$$

$$\text{where } \mathbf{l}_d = (l_d, m_d, (n_d - 1)) \quad (3.28)$$

$$\boldsymbol{\delta u}_{bb'} = (\delta u_{bb'}, \delta v_{bb'}, \delta w_{bb'}) \quad (3.29)$$

$$= (u_b - u_{b'}, v_b - v_{b'}, w_b - w_{b'}) \quad (3.30)$$

In Eq 3.27, we have:

$$\text{Diag}\{\mathcal{F}_{bb'}\}[d] = e^{2i\pi \mathbf{l}_d \cdot \boldsymbol{\delta u}_{bb'}} \quad (3.31)$$

For $b \neq b'$, the diagonals of $\mathcal{F}_{bb'}$ are the Fourier kernels mapping $\delta u \delta v$ space to $\delta l \delta m$. $\mathcal{F}_{bb'}$ can then be thought of as a Fourier transform. It is not a diagonal matrix. It behaves as a *covariance fringe*, allowing us to extend standard interferometric ideas to covariance space: each fringe can be thought of as a single “spatial filter” applied to the pixel covariance matrix. Just as a given baseline has coordinates in *uv*-space, a given *correlation between baseline residual errors* has coordinates in *uv correlation space*, which we will henceforth refer to as $\delta u \delta v$ -space.

This $\delta u \delta v$ space warrants further discussion: Fig. 3.1 shows, for a given *uv*-track (Fig. 3.1b), both the corresponding $\delta u \delta v$ domain (Fig. 3.1c) and point-spread function (Fig. 3.1a). The symmetric, negative *uv*-track is treated as a separate track, and thus ignored. This means that we do not fully constrain the noise-PSF (since the covariance matrix of the symmetric track is simply the Hermitian of the first), but we do not seek to constrain it in this section, but rather to show that our results hold.. We can see that the $\delta u \delta v$ -tracks are symmetrical about the origin. The $\delta u \delta v$ space corresponding to a given *uv*-track can thus be most concisely described as a “filled *uv*-track”, with its boundaries defined by the ends of the *uv*-track. The set of $\mathcal{F}_{bb'}$, each of which maps one value of the covariance matrix to a fringe in the image-plane, would then characterise a PSF equivalent for the noise distribution, which we refer to as the noise-PSF. In our formalism, the only source of statistical effects in the field are calibration errors and thermal noise. The average variance in all pixels will be given by the diagonal of

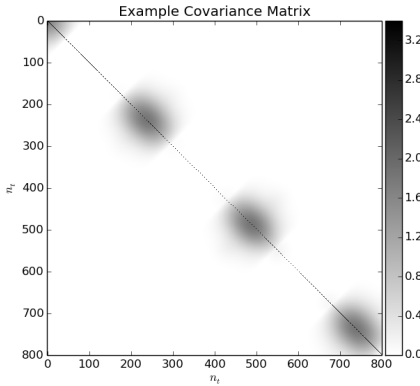


Figure 3.2. Example of a non-stationary covariance matrix, which can be used to simulate $\text{Cov}\{\tilde{\gamma}\}$. The colourbar units are Jy^2 . The correlation scale σ_τ is 40 cells, and the variability period is 500 cells. The matrix is made positive semi-definite (and therefore a covariance matrix) through SVD decomposition. The maximum size of the “bubbles” is determined by σ_τ .

the covariance matrix and the thermal noise, provided that it truly follows a normal distribution. The only effects which will cause the variance in the image-plane to vary from one pixel to the next are those mapped onto the covariance fringes, i.e. such position-dependent variance fluctuations will be caused by correlated gain errors, which are spurious signal introduced by erroneous gain estimates. Assuming all sources in the field are point-like and distant, then these variance fluctuations will follow a specific distribution, convolved to every source in the field. Since the variance fluctuations act as tracers for calibration artefacts, artefacts in the image can be understood as *one realisation* of the variance map, which is characterised by an average level determined by the variance in the gains and thermal noise, and a noise-PSF convolved with the sky brightness distribution. The actual artefacts in the image will still be noisy, as a realisation of the true variance map. For the same reason, in the absence of correlated gain errors, $[\text{Cov}\{\tilde{\gamma}\}]_{b \neq b'}$ are all zero and $\text{Cov}\{\tilde{\gamma}\}$ is a diagonal matrix. We then recover a “flat” noise-map: the variance will be the same in all pixels, as the noise-PSF is absent. In the ideal case, were we to recover the true value of the gains for all times and frequencies, this becomes pure thermal noise.

3.3.3 Noise Map Simulations

We have shown in Eq. 3.25 that there exists an analytical relationship between residual visibility statistics and image-plane residual statistics. This section gives details of simulations we have performed to support our claims on this “Cov-Cov” relationship. Specifically, we simulate residual visibilities for a single baseline by generating a set of correlated random numbers with zero mean and a distribution following a specified covariance matrix \mathbf{C} . It contains a periodic function of period T along the diagonal, which is then convolved with a Gaussian of width σ_τ corresponding to the characteristic scale of correlation. The values of these parameters are chosen arbitrarily. A small constant term is added on the diagonal, the net value of which is strictly positive. This simulates a low thermal noise. Finally, singular value decomposition is used to ensure that this matrix is Hermitian positive semi-definite. The net effect is a non-stationary

correlation: some residuals are correlated with their neighbours, and uncorrelated with others. An example of this covariance matrix for arbitrary parameter values is shown in Fig. 3.2. We see that, for any given point, correlation is stronger with some neighbours than others (as determined by σ_τ). Samples are drawn as follows: \mathbf{C} is built following user specifications as described above. We then find its matrix square root \mathbf{C}_0 so as to apply it to random numbers generated from a normal distribution. We generate 2000 realisations i of our random variables \mathbf{r}_i :

$$\tilde{\mathbf{y}}_i = \sum_b \mathcal{F}_{bi} \mathbf{r}_i \quad \text{with} \quad \mathbf{r}_i = \mathbf{C}_0 \mathbf{x} \quad (3.32)$$

$$\text{and} \quad \mathbf{x} \leftarrow \mathcal{N}(0, 1) \quad (3.33)$$

$$\tilde{\mathbf{y}} = (\cdots \tilde{\mathbf{y}}_i \cdots) \quad (3.34)$$

where $\tilde{\mathbf{y}}$ is a matrix of dimensions $n_{\text{realis}} \times n_b$. Since \mathbf{x} follows a normal distribution, $\text{Cov}\{\mathbf{x}\} = \mathbf{I}$ and the covariance matrix of each $\tilde{\mathbf{y}}_i$ is, by construction, $\mathbf{C} = \mathbf{C}_0 \mathbf{C}_0^H$. The covariance matrix of $\tilde{\mathbf{y}}$ is thus also \mathbf{C} .

As for the *uv*-track, our simulations read a single one from a specified dataset. In this case, we read an 8-hour *uv*-track for a baseline between two arbitrary LOFAR stations (specifically, CS001HBA0 and RS310HBA) in an observation of the Boötes extragalactic field. The effective baseline length varies between 37.9km and 51.8km. The dataset included 20 channels, each with a spectral width of 97.7 kHz; the central observing frequency is 139 MHz. The temporal resolution is 1 measurement per second.

We compare the *measured* variance map $\mathbf{V}_{\tilde{\mathbf{y}}}^m$, built by measuring the variance across realisations at each pixel in the image-plane, with the *predicted* variance map $\text{Var}\{\tilde{\mathbf{y}}\}$, built using the Cov-Cov relationship (Eq. 3.25). Since we are only interested in the variance map, rather than the covariance between pixels, we compute only the diagonal terms.

$$\mathbf{V}_{\tilde{\mathbf{y}}}^m = \text{Diag}\{\tilde{\mathbf{y}} \tilde{\mathbf{y}}^H\} \quad (3.35)$$

$$\mathbf{V}_{\tilde{\mathbf{y}}}^{pr} = \sum_b [\mathbf{C}]_{bb} \mathbf{I} + \sum_{b,b' \neq b} \text{Diag}\{\mathcal{F}_{bb'}\} [\mathbf{C}]_{bb'} \quad (3.36)$$

where the thermal noise is already incorporated into the diagonal of \mathbf{C} and Eq. 3.36 is merely the diagonal operator applied to the Cov-Cov relationship.

Simulation with a single point source

We model our sky as containing a single 1 Jy point source at phase centre: we thus have $\phi_{bb} = w_b^2$. The source as seen through the set of *uv*-tracks used in our simulation, along with their corresponding $(\delta u, \delta v)$ space, are shown in Fig. 3.1. The *simulated* noise-map is calculated by drawing a large sample ($n_{\text{realis}} = 2000$) of random numbers from the correlated distribution, thereby creating 2000 sets of residual visibilities. By Fourier-transforming the visibilities to the image-plane and taking the variance of the values for each image pixel (i.e. each l, m pair) as per Eq. 3.35, we can estimate $\text{Var}\{\tilde{\mathbf{y}}\}$. The *predicted* noise-map, meanwhile, was found by assigning each cell of \mathbf{C} to the appropriate point in the $(\delta u, \delta v)$ plane and Fourier transforming from this plane into the image-plane, as per Eq. 3.36. We compare the outcome of simulating a large number n_{realis} of realisations and taking the variance across these realisations for each pixel with

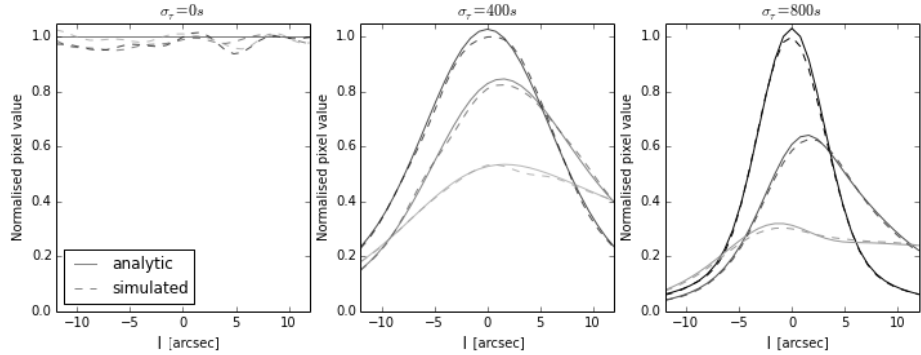


Figure 3.3. The three lines in each figure correspond to three horizontal cross-sections from images in Fig. 3.4. The units on the y-axis are dimensionless [Jy^2/Jy^2]. σ_τ is the maximum characteristic error correlation length. In decreasing intensity, they correspond to $m = 0''$, $m = 4''$, and $m = 8''$. The dashed lines correspond to the variance measured with 2000 realisations for each pixel, while the solid line corresponds to the predicted value at that pixel. There are 31 pixels. We do not show cross-sections for negative m due to image symmetry about the origin.

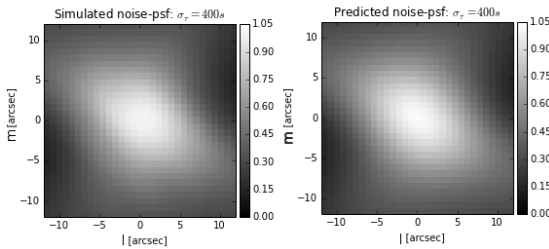


Figure 3.4. Simulated noise-maps, compared with theoretical prediction. The pixel values are normalised by the average value of the covariance matrix: the units of the colourbar are thus dimensionless (Jy^2/Jy^2). These are on the same angular scale as the source shown in Fig. 3.1.

mapping the covariance matrix onto the $\delta u \delta v$ -plane and using the Cov-Cov relationship. The results of our simulations are shown side-by-side in Fig. 3.4: the predicted and simulated noise-PSFs match. The peak-normalised predicted noise-PSF is less noisy, as shown in Fig. 3.3 for different correlation scales. This is expected, since it is calculated directly from the underlying distribution, rather than an estimate thereof. As $n_{\text{realis}} \rightarrow \infty$, we expect the two methods to fully converge. As the maximum characteristic correlation length σ_τ increases, the variance becomes ever more sharply peaked.

Since our simulated sky consists of a 1Jy source at phase centre, there is only one noise-PSF to modulate the average noise level, and it lies at phase centre. Let us test our formalism further by considering a model with multiple point sources.

Simulation with 3 point sources

We wish to test our prediction that the noise-map can be described as a convolutional process modulating an average noise level. We thus perform another simulation, this time with three 1Jy point sources. The associated dirty image is shown in Fig. 3.5d.

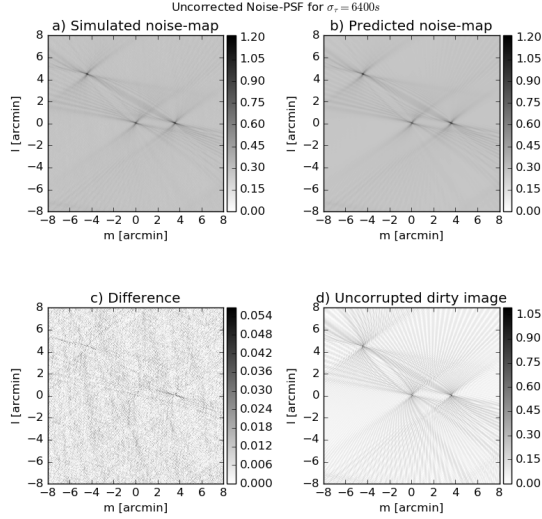


Figure 3.5. Noise-map of sky with correlated gain errors and three point sources. The colourbars of (a), (b) and (c) have dimensionless units, while that of (d) is in Jansky. Note the presence of structure in the residuals (c): these show the limits of our hypothesis that sources are spatially incoherent.

This dirty image simply consists of performing a direct Fourier transform (i.e. without using a Fast Fourier Transform algorithm) on simulated visibilities corresponding to these three point sources. We now perform a similar test as above on this field. Firstly, we “apply” gain errors to these visibilities by multiplying our model with our residual gain errors. This allows us to find 2000 realisations of residual visibilities, and find the variance for each pixel across these realisations. This gives us the simulated noise-map, shown in Fig. 3.5a. Secondly, we perform a DFT from the differential Fourier plane to the (l, m) plane as before, assigning one cell of $\text{Cov}\{\tilde{\gamma}\}$ to each point of the differential Fourier plane. This time, however, ϕ_{bb}^d is not simply unity for all points in the differential Fourier plane. Instead, it is calculated for the three-point-source model, and applied for each point. This gives us the predicted noise-map in Fig. 3.5b. Finally, Fig. 3.5c shows the absolute value of the difference between the two images. We see that there is some structure present in these residuals: this is expected, as the PSF of the sources in the dirty images clearly overlap. We are thus not quite in the regime where emission is fully spatially incoherent. Nevertheless, our predictions hold to better than 5% accuracy.

It bears repeating that, for correlated noise, this map can be understood as a distribution map for calibration artefacts: the amount of spurious correlated emission seen by each baseline will determine the noise-map, and the true image-plane artefacts will then be *one set of realisations* of this *underlying distribution*.

3.4 Adaptive Quality-based Weighting Schemes

As discussed in Section 3.2, some intervals of an observation will have lower gain variability. These will show up in the gain covariance matrix as intervals with lower variance. Similarly, those with larger intrinsic gain variability will have greater error in

their gain estimate. By giving greater weights to the former, and lower weights to the latter, we expect to be able to improve image reconstruction. We thus talk of adaptive quality-based weighting, as the weights will adapt based on the calibration quality.

The pixel variance is determined by the visibility covariance matrix, as shown in Eq. 3.27. The diagonal of the visibility covariance matrix will add a flat noise to all pixels, while its wings will determine the calibration artefact distribution, which will be convolved to the sky brightness distribution. We thus have two sources of variance in the image-plane. Minimising the far-field noise (i.e. the variance far from sources) in an image would involve down-weighting noisier calibration intervals while up-weighting the more quiescent ones, without taking noise-correlation between visibilities into account. This is because the far-field noise will be dominated by the diagonal component of the covariance matrix (cf. Eq. 3.27). By the same token, minimising calibration artefacts would involve down-weighting measurements with strongly-correlated noise, and up-weighting the less-correlated. This would not, however, minimise the diagonal component: in fact, it will likely exaggerate its up-weighting and down-weighting. As such, it will increase the constant level of the noise-map, but flatten the noise-PSF's contribution. There are thus two competing types of noise that we seek to minimise: uncorrelated noise, which corresponds to $\delta u \delta v = 0$ (i.e. the diagonal components of the gain covariance matrix), and correlated noise, which corresponds to $\delta u \delta v \neq 0$ (i.e. its wings). Minimising the first will minimise far-field noise without optimally reducing artefacts, while minimising the last will minimise noise near sources at a cost to far-field noise. In the following sub-sections, we will discuss weighting schemes used to accomplish this.

3.4.1 Optimising sensitivity

The Cov-Cov relationship (Eq. 3.25) tells us that, far from any sources, the variance map (Eq. 3.27) is dominated by a constant term: the contribution from thermal noise and the diagonal of the residual visibility covariance matrix. Maximising sensitivity far from sources therefore implies minimising $\text{Diag}\{\text{Cov}\{\tilde{\gamma}\}\}$. This is equivalent to assigning visibilities weights inversely proportional to their variance:

$$w_b = \frac{1}{\text{Var}\{\tilde{\gamma}_b\}} \quad (3.37)$$

For each baseline, those times with larger variance in the residuals will be down-weighted, and those with smaller variance will be up-weighted; this scheme does not require information about the underlying gains, only the error on our solutions. Since we are treating σ_n^2 as a constant for all antennas and all times, those times where our gains estimate is closer to the true gains will be up-weighted, and those moments where they are farther from the actual gains will be down-weighted: hence the term “adaptive quality-based weighting”. Note that the diagonal of the weighted residuals’ covariance matrix should therefore become constant: this weighting scheme explicitly brings the residuals closer to what is expected in the case of perfect calibration, assuming uncorrelated noise. For the remainder of this paper, we will refer to these weights as *sensitivity-optimal* weighting.

3.4.2 Minimising Calibration Artefacts

Minimising calibration artefacts - i.e. optimising the sensitivity near bright sources - means flattening the noise-map. Since the noise-map can be understood as a noise-PSF convolved with all the modeled sources in the sky modulating the background variance level, it will be flattest when its peak is minimised. From the Cov-Cov relationship (Eq. 3.25), we can see that, at the peak of the noise-PSF (which would be the variance at the pixel where $l = m = 0$), the Fourier kernel is unity: the variance for that pixel is thus the sum of all the cells in the covariance matrix. By accounting for normalisation, we can write the variance at the centre of the noise-PSF as:

$$V(\mathbf{w}) = \frac{\mathbf{w}^T \text{Cov}\{\tilde{\gamma}\} \mathbf{w}}{\mathbf{w}^T \mathbf{1} \mathbf{1}^T \mathbf{w}} \quad (3.38)$$

Our optimality condition is then, after some algebra:

$$0 = \frac{\partial}{\partial \mathbf{w}} (V) \quad (3.39)$$

$$\Leftrightarrow \text{Cov}\{\tilde{\gamma}\} \mathbf{w} = \mathbf{1} \mathbf{1}^T \mathbf{w} (\mathbf{w}^T \mathbf{1} \mathbf{1}^T \mathbf{w})^{-1} \mathbf{w}^T \text{Cov}\{\tilde{\gamma}\} \mathbf{w} \quad (3.40)$$

We find that one \mathbf{w} which satisfies the above is:

$$\mathbf{w} = \text{Cov}\{\tilde{\gamma}\}^{-1} \mathbf{1} \quad (3.41)$$

where $\mathbf{1}$ is a vector of ones. These weights depend only on calibration quality: badly-calibrated cells will include spurious time-correlated signal introduced by trying to fit the noise n on visibilities. Down-weighting these cells helps suppress artefacts in the field, at the cost of far-field sensitivity. This weighting scheme is thus only a function of the relative quality of calibration at different times, boosting better-calibrated visibilities and suppressing poorly-calibrated visibilities. For the remainder of this paper, we will refer to these weights as *artefact-optimal* weighting.

3.5 Estimating the Covariance Matrix

In our simulations, we have worked from a known covariance matrix and shown that our predictions for the residual image's behaviour hold. With real data, however, we do not have access to this underlying covariance matrix. Since our weights are extracted from said matrix, estimating it as accurately as possible remains a challenge: this is in turn limited by the number of samples which can be used for each cell.

Each cell in the covariance matrix is built by averaging a number of measurements, or samples. The more samples are available, the better our estimate becomes: once we have more samples than degrees of freedom, we say that our estimation is well-conditioned. Otherwise, it is poorly-conditioned. In this section, we will discuss ways in which we can improve the conditioning of the covariance matrix estimation.

3.5.1 Baseline-based Estimation

One way to improve the conditioning of our covariance matrix estimation is to make the same hypothesis as the calibration algorithm: we can treat the underlying gains as

constant within each calibration interval. Provided this interval is known, this allows us to find a single estimate for each interval block of the covariance matrix, turning a $n_b \times n_b$ matrix into a smaller $n_{\text{intervals}} \times n_{\text{intervals}}$ equivalent, where $n_{\text{intervals}}$ is the number of solution intervals used for to find the gain solutions. We then improve our conditioning by a factor of n_{int} , which is the number of samples in a calibration interval. The estimate $\widehat{\text{Cov}\{\tilde{\gamma}\}}$ of the covariance matrix $\text{Cov}\{\tilde{\gamma}\}$ is built by applying the covariance operator:

$$\widehat{\text{Cov}\{\tilde{\gamma}\}} \stackrel{\text{def}}{=} \widehat{\mathbf{C}_{\tilde{\gamma}}} = \frac{1}{n_{\text{int}}} \sum_{i \in n_{\text{int}}} (\tilde{\gamma}_i - \langle \tilde{\gamma} \rangle) (\tilde{\gamma}_i - \langle \tilde{\gamma} \rangle)^H \quad (3.42)$$

where the $\langle \dots \rangle$ operator denotes taking the average over the full vector. If the calibration solver's gain estimates are unbiased (i.e. $E\{\hat{\mathbf{g}}\} = \mathbf{g}$) and the model of the sky is sufficiently complete, this quantity should be zero. Having created $\widehat{\mathbf{C}_{\tilde{\gamma}}}$, which will be of size $n_b \times n_b$, its cells can now be averaged over blocks of $n_{\text{int}} \times n_{\text{int}}$. This allows us to estimate the weights for each baseline and each time.

Mathematically, we retrace the steps of Section 3.3. In the absence of direction-dependent effects, we define the residual visibilities as before, and use them to define the normalised residual visibilities ρ_b :

$$r_b = w_b \kappa_b \tilde{\gamma}_b + \epsilon \quad (3.43)$$

$$\rho_b = \frac{r_b}{k_b} \quad (3.44)$$

We then organise the residuals in cells:

$$\mathbf{r}_{\mathcal{C}} = \begin{pmatrix} \vdots \\ \rho_{b \in \mathcal{C}} \\ \vdots \end{pmatrix} \quad (3.45)$$

$$\mathbf{R} = (\dots \quad \mathbf{r}_{\mathcal{C}} \quad \dots) \quad (3.46)$$

\mathbf{R} corresponds to a matrix containing all the residual visibilities within one calibration cell \mathcal{C} , i.e. for $b \in \mathcal{C}$ where $\mathbf{g}_{\mathcal{C}} = \text{const}$. It is therefore of size $n_{\text{intervals}} \times n_{\mathcal{C}}$, where $n_{\text{intervals}}$ is the number of calibration intervals in the observation. Normalising the residual visibilities by k_b allows us to recover the underlying covariance matrix by multiplying the residual visibility matrix \mathbf{R} with its Hermitian conjugate:

$$\widehat{\mathbf{C}}_{\tilde{\gamma}}[b \in \mathcal{C}, b' \in \mathcal{C}'] = (\mathbf{R}^H \mathbf{R})[\mathcal{C}, \mathcal{C}'] \quad (3.47)$$

Note that we have divided the noise term by the flux model S_b , which can be very small in some cells. As such, care must be taken not to cause the relative thermal noise contribution to explode: those cells where this would occur are dominated by thermal noise, and information on the covariance matrix cannot be recovered from them.

In this framework, we simply treat the index \mathcal{C} as containing all the times and frequencies, for individual baselines, corresponding to a single calibration interval. $\widehat{\mathbf{C}}_{\tilde{\gamma}}$ is then an estimate of the residual visibility covariance matrix.

3.5.2 Antenna-based Estimation

In the subsection above, we assumed that finding one solution per interval will give us strong enough constraints to make the problem of estimating the covariance matrix well-conditioned: this may not be true in all cases. Conditioning may then need to be improved further: in this subsection, we show one way in which this can be done. There are others, e.g. using the rank of the matrix itself to find better-conditioned estimates of the covariance matrix at a lower resolution (i.e. a single estimate for a greater number of cells). They will not be presented in this paper, but are a possible avenue future work on this topic.

In estimating the covariance matrix for each baseline and each calibration cell, we are severely limited by the small number of samples in each cell. One way to overcome this problem is to find estimates for the variance of *antenna* gains, and use these to return to the baseline variances. In this formalism, we extend \mathcal{C} to include all visibilities pointing at a single antenna at a given time. Let us begin by writing an expression for the gain vector, which contains the gains for all antennas and all calibration cells:

$$\hat{\mathbf{g}}_c = \begin{pmatrix} \vdots \\ \hat{g}_p^{\tau \in c} \\ \vdots \end{pmatrix} \quad (3.48)$$

$$\hat{\mathbf{G}} = (\dots \quad \hat{\mathbf{g}}_c \quad \dots) \quad (3.49)$$

and the variance on each antenna in each calibration cell is then:

$$= E\{\hat{\mathbf{g}}_c \hat{\mathbf{g}}_c^H\} - \underbrace{E\{\hat{\mathbf{g}}_c\} E\{\hat{\mathbf{g}}_c\}^H}_{=\mathbf{g}_c \mathbf{g}_c^H} \quad (3.50)$$

As we can see, Eq. 3.50 is simply a vector form of Eq. 3.12. The residual gains of Eq. 3.12 can now be understood as random samples of the covariance between the gains for antennas p and q at a given time, assuming complete skymodel subtraction. We can thus define the variance sample matrix as an *estimate* of the *variance matrix*:

$$\widehat{\mathbf{V}}_{\mathcal{C}} = \widehat{\text{Var}\{\mathbf{g}_c\}} \quad (3.51)$$

$$= \sum_{\tau \in \mathcal{C}} (\hat{\mathbf{g}}_{\tau} \hat{\mathbf{g}}_{\tau}^H - \mathbf{g}_{\tau} \mathbf{g}_{\tau}^H) \quad (3.52)$$

We define the residual matrix as:

$$\mathbf{r}_{\tau} = \sum_d s_d \mathbf{K}_{d,\tau} (\hat{\mathbf{g}}_{\tau} \hat{\mathbf{g}}_{\tau}^H - \mathbf{g}_{\tau} \mathbf{g}_{\tau}^H) \mathbf{K}_{d,\tau}^H + \epsilon \quad (3.53)$$

where we explicitly place ourselves in the limits of our formalism, i.e. that we do not have direction-dependent gains. We now see that at the core of Eq. 3.53 lies $\widehat{\mathbf{V}}_{\hat{\mathbf{g}}_{\tau}}$, where $\sum_{\tau \in \mathcal{C}} \widehat{\mathbf{V}}_{\hat{\mathbf{g}}_{\tau}} = \widehat{\mathbf{V}}_{\mathcal{C}}$. The K-matrix is defined as follows:

$$\mathbf{K}_{d,\tau} = \begin{pmatrix} k_{p,\tau}^d & 0 & \\ 0 & k_{q,\tau}^d & \\ & & \ddots \end{pmatrix} \quad (3.54)$$

Since the residual matrix depends on the gains, we define the residual visibility vectors as:

$$\mathbf{r}_{\mathcal{C}} = \begin{pmatrix} \vdots \\ \mathbf{r}_{\tau \in \mathcal{C}} \\ \vdots \end{pmatrix} \quad (3.55)$$

$$\mathbf{R} = (\dots \quad \mathbf{r}_c \quad \dots) \quad (3.56)$$

$\mathbf{r}_{\mathcal{C}}$ corresponds to a matrix containing all the residual visibilities within one calibration cell \mathcal{C} , i.e. for $\tau \in \mathcal{C}$ where $\mathbf{g}_{\mathcal{C}} = \text{const}$. Let us define $n_{\mathcal{C}}$ as the number of elements in each calibration cell. The residual variance sample matrix can now be built by multiplying the residual visibility matrix with its Hermitian conjugate:

$$\mathbb{V} = \mathbf{R}^H \mathbf{R} \quad (3.57)$$

Note that we do this because it allows us to turn a single noise realisation ϵ into a statistical quantity σ . We can relate \mathbb{V} to the variance of individual antenna gains:

$$\mathbb{V} = \sum_{\tau \in \mathcal{C}} \left(\sum_{d, d'} s_d \mathbf{K}_{d, \tau} (\widehat{\mathbf{V}}_{\mathcal{C}})^H \mathbf{K}_{d, \tau}^H s_{d'} \mathbf{K}_{d', \tau} (\widehat{\mathbf{V}}_{\mathcal{C}}) \mathbf{K}_{d', \tau}^H + \mathbf{I} \sigma^2 \right) \quad (3.58)$$

To reach this point, in Eq. 3.23, we made the hypothesis that the sky brightness distribution is dominated by spatially incoherent emission. Applying this hypothesis again here, we can make the approximation that the cross-terms in the sum over d, d' average to zero: $\sum_{d, d' \neq d} \approx 0$. We then have:

$$\mathbb{V} \approx \sum_{\tau} \left(\sum_d s_d^2 \mathbf{K}_{d, \tau} (\widehat{\mathbf{V}}_{\mathcal{C}})^H (\widehat{\mathbf{V}}_{\mathcal{C}}) \mathbf{K}_{d, \tau}^H + \mathbf{I} \sigma^2 \right) \quad (3.59)$$

$$= (\widehat{\mathbf{V}}_{\mathcal{C}})^2 \circ \underbrace{\left(\sum_{\tau} \sum_d s_d^2 \mathbf{k}_{d, \tau} \mathbf{k}_{d, \tau}^H \right)}_{\stackrel{\text{def}}{=} \mathcal{S}} + n_{\mathcal{C}} \mathbf{I} \sigma^2 \quad (3.60)$$

$$\widehat{\mathbf{V}}_{\mathcal{C}} = \sqrt{\mathcal{S}^{\circ -1} (\mathbb{V} - n_{\mathcal{C}} \mathbf{I} \sigma^2)} \quad (3.61)$$

where \circ denotes the Hadamard or entrywise product and $\mathbf{k} = \text{Diag}\{\mathbf{K}\}$. Thus, \mathbb{V} allows us to estimate the variance of each antenna and for each calibration cell by using all the visibilities pointing to that antenna within that calibration cell. With this information, we can then rebuild the baseline-dependent matrix, having improved our sampling by a factor of n_{ant} .

3.6 Applying the Correction to Simulated Data

In this section, we show the impact of our weighting schemes on a noise-map made from arbitrarily strongly-correlated residuals. Here, we assume that our sky contains only a single point source at phase centre: there is thus only a single instance of the noise-PSF, placed at phase centre, to modulate the average variance level. We sample this instance

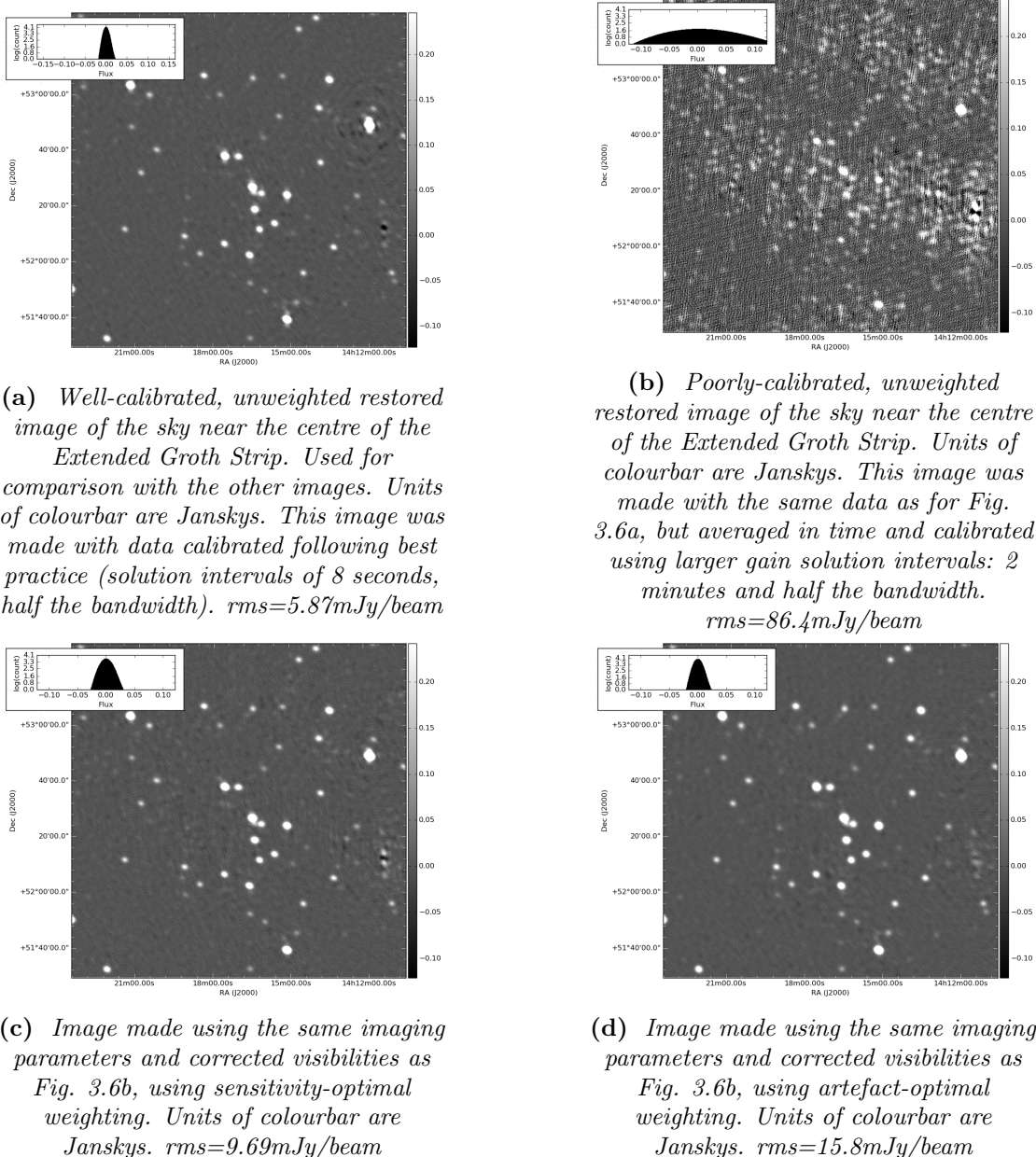


Figure 3.6. Restored images of the centre of the Extended Groth Strip, as seen with an 8-hour observation using the full LOFAR array. Fig. 3.6a shows an image of the field made with good calibration intervals. Fig. 3.6b shows an image of the field made with poor calibration intervals. Fig. 3.6c shows image made with the same visibilities and imaging parameters, but with the application of the sensitivity-optimal weighting scheme. Fig. 3.6d, similarly, differs from Fig. 3.6c only in that artefact-optimal weights, rather than sensitivity-optimal weights, were used. The histograms of pixel values in each image have 1000 flux bins ranging from -0.16 Jy to 0.16 Jy. Their ordinates are in log scale. Pixel size is 1.5" in all images.

by taking a cross-section from $(l, m) = 0$ to a large l , keeping m constant. The only difference between these cross-sections is the weighting scheme applied: unit weights for all visibilities (“Uncorrected”, blue), sensitivity-optimal weights (green), and artefact-

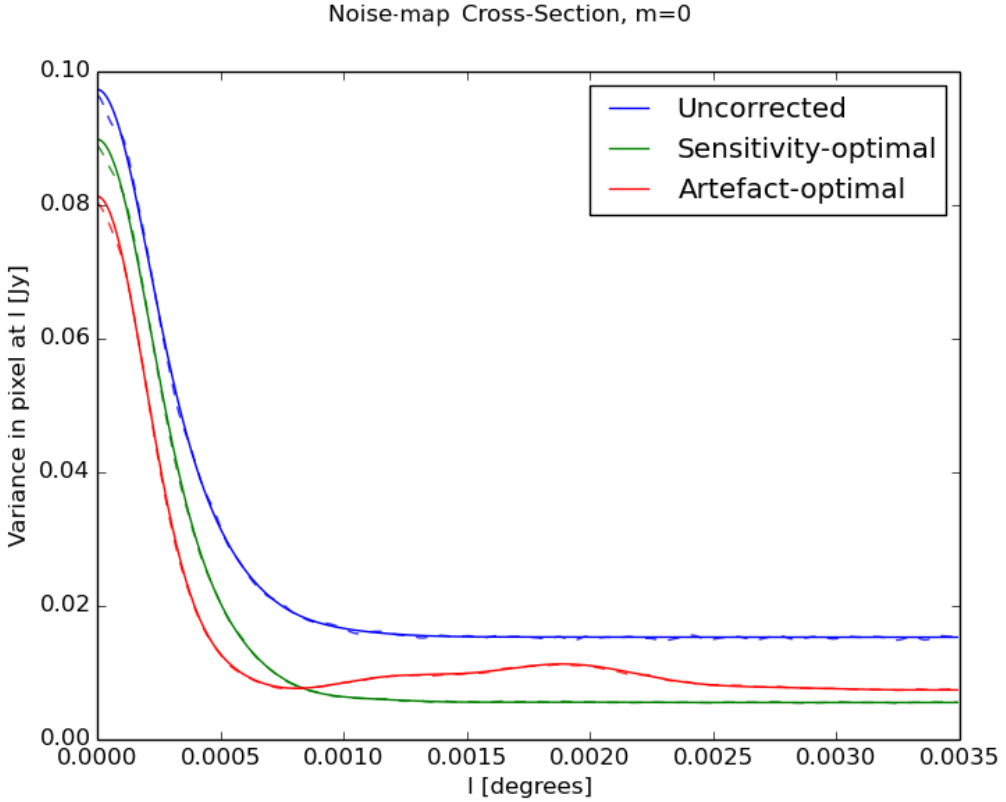


Figure 3.7. The sensitivity-optimal (green) and artefact-optimal (red) weights both give improvements over the unweighted noise-map (blue).

optimal weights (red). We plot both the result predicted by the Cov-Cov relationship (solid line) and the variance estimated across 2000 realisations (dashed line): the result is shown in Fig. 3.7. The two remain in such agreement throughout the cross-section as to be nearly indistinguishable.

There are a few significant points to note on this figure. Firstly, most of the power in the matrix lies along the diagonal: both weighting schemes thus give good improvements in variance across the map. The artefact-optimal weights, while decreasing the peak further, as expected, also increases the noise far from sources: this is due to the fact that the artefact-optimal weights are in a sense more “selective” than the sensitivity-optimal weights: they up-weigh and down-weigh more severely, and will only result in a constant covariance matrix if this matrix is zero everywhere outside of the diagonal. In effect, the noise-map becomes flatter, but much broader.

3.7 Applying the Correction to Real Data

In this section, we show the effect of adaptive quality-based weighting on real data. The dataset used in this section is a single sub-band from an 8-hour LOFAR observation centred on the Extended Groth Strip ($\alpha=14:19:17.84, \delta=52:49:26.49$). The observation was performed on August 28th, 2014. The subband includes 8 channels of width 24.414

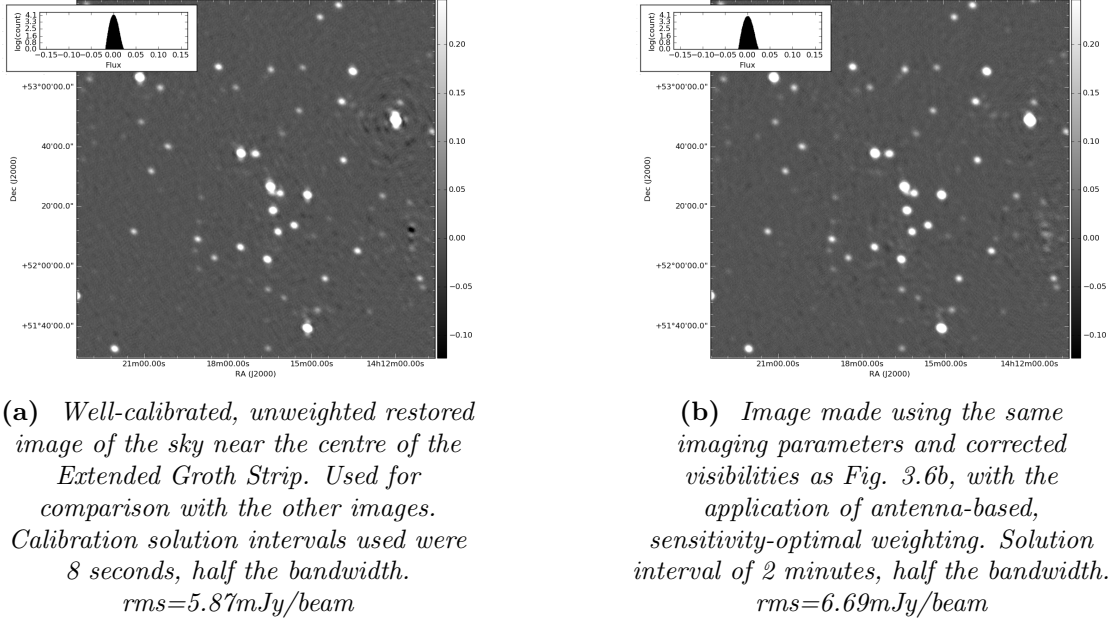


Figure 3.8. Comparison between the well-calibrated image (i.e. the same image as Fig 3.6a) and antenna-based sensitivity-optimal weights. Units of both colourbars are Jansky. We see that we recover a very similar image, despite the fact that the data used for the weighted image are averaged by a factor of 8 compared to those used for the unweighted image.

kHz each, for a total bandwidth ranging from 150.2 to 150.5 MHz. The data have been averaged in time to 1 data point per second. The data was calibrated using Wirtinger calibration (see Tasse 2014; Smirnov & Tasse 2015, and references therein) and a sky model consisting only of a nearby calibrator source, 3C295. A reference image (a cutout of which is shown in Fig. 3.6a) was made by calibrating the data according to best practice for LOFAR survey data: 1 calibration solution per 8 seconds and per 4 channels. The residual data was then corrected by the gain solutions and imaged using Briggs weighting (robust=0), pixel size of $1.5''$, and deconvolved using the default devoncolution algorithm in DDFacet (Tasse et al., in press).

The data was then time-averaged to create a new, 2.4 GB dataset with 1 data point per 8 seconds. Deliberately poor calibration was then performed on this dataset, solving for 1 calibration solution per 2 minutes (*caeteris paribus*). The resulting corrected residual data was imaged using the same imaging parameters as the reference image, and a cutout of the result is shown in Fig. 3.6b. As expected, the very long calibration intervals introduce calibration artefacts in the image. The brightest sources are still visible, but much of the fainter emission is buried under these artefacts. We are then in a case where our residual visibilities are dominated by calibration error rather than sky model incompleteness.

Weights were then calculated based on the badly-calibrated residual visibilities. Fig. 3.6c was made using the same visibilities as Fig. 3.6b and applying baseline-based, sensitivity-optimal weight. Similarly, Fig. 3.6d used the poorly-calibrated residual visibilities with the application of baseline-based, artefact-optimal weighting. These weights

are likely to be poorly-conditioned. In both cases, all other parameters were conserved.

Note that applying antenna-based sensitivity-optimal weighting to the badly-calibrated data (not shown here) allows us to recover the reference image with only a very small increase in rms (increased by a factor of 1.14). Further testing on complex field simulations will be required to ascertain the usefulness of artefact-optimal weighting: it is likely that it fails to correct the image fully due to the poor conditioning of the covariance matrix used here.

The pixel histograms show us that the weights do not completely mitigate the poor calibration interval choice, but certainly give a dramatic improvement over the unweighted, poorly-calibrated residuals. This is compatible with our statement that the weights give similar residuals in the image with a dramatic improvement in time at some cost in sensitivity. It is interesting to note that while Fig. 3.6d looks noisier than Fig 3.6c, its residual flux histogram is actually closer to that of Fig. 3.6a.

As for performance, the weights used for Fig. 3.6d took 8 hours of computing time on a single core⁴, working on a 29 GB dataset, which is not particularly large for LOFAR data. Since the problem is massively parallel, this cost can be alleviated. The main bottleneck is likely due to very poor code optimization. As for the weights used for Fig. 3.8b, they are computed in 1min6s on the same single core.

3.8 Discussion

This paper began by investigating the use of an algorithm inspired by “lucky imaging” to improve images made using radio interferometric data. By investigating the statistics of residual visibilities, we have made the following findings:

- A relationship between the statistics of residual visibilities and residual pixel values (the “Cov-Cov relationship”).
- A description of the noise-map in the image plane as a constant variance level modulated by a noise-PSF convolved with the sources in the field. This gives the variance in the flux of the image as a function of distance from the sources in the sky for a given calibration.
- An Adaptive Quality-Based weighting scheme, which reduces the noise in the image (and the presence of calibration artefacts) by minimising either the constant noise term or the noise-PSF.

While our results are not a panacea for poor calibration, they show that we can not only improve images made with well-calibrated data, but also mitigate the worst effects of poorly-calibrated visibilities in otherwise well-calibrated datasets. Provided that the gain variability timescale is long enough at certain points of the observation, we can effectively get images of similar quality using both the “standard” best-practice calibration interval for LOFAR survey data (calibration solution interval of 8 seconds)

⁴Core type: Intel(R) Xeon(R) CPU E5-2660 0 @ 2.20GHz

and a significantly larger solution interval of 2 minutes (frequency interval unchanged). Of course, if no such stable interval exists, there will be no good intervals to upweigh, and we will be left only with equally-poor data chunks. This means that, in the right conditions, net pipeline time can be sped up by a factor of nearly three, at a slight cost in sensitivity. This increase will be greater than what could be achieved with existing comparable methods such as “clipping”.

We emphasize that the adaptive quality-based weighting schemes work because the noise-map describes the *underlying noise distribution*, of which calibration artefacts are *one single realisation*. To fully characterise the artefacts, the correlation between different pixels (i.e. off-diagonal elements of $\text{Cov}\{\tilde{\mathbf{y}}\}$) must be computed; this has not been done in this paper. Nevertheless, lesser constraints on the spatial distribution of artefacts can be found using only the diagonal elements of $\text{Cov}\{\tilde{\mathbf{y}}\}$. The weighting schemes merely seek to minimise this spatial distribution as much as possible: the end result is *fewer artefacts*, which can be distributed across a *much larger area*. This is the source of the dramatic improvement from 3.6b to Fig. 3.6c. We have simply down-weighted those visibilities where spurious signal was introduced by the calibration solutions, and up-weighted those visibilities where such signal was lesser. Since this spurious signal is the source of calibration artefacts, downweighting the associated visibilities reduces it dramatically. The poor improvement from Fig. 3.6b to 3.6d is likely due to limits in the conditioning of our estimation of the covariance matrix.

The work presented here can be improved upon, notably by working on improving the conditioning of our covariance matrix estimate: for real observations, it is impossible to have more than one realization of each gain value for all antennas. By treating each visibility within a calibration interval as a realization of the true distribution, we can better estimate the covariance matrix per baseline, and thus reach a better estimate of the variance in the image-plane. Of course, in practice, we can never access to the true, underlying time-covariance matrix for each baseline. Significant hurdles remain:

- The impact of sky model incompleteness (since calibration requires a sky model) is ignored in this paper; we start by assuming that we have a complete sky model. In practice, of course, acquiring a complete sky model is often a key science goal in and of itself. The impact of this hypothesis therefore ought to be investigated in future work.
- The conditioning of our covariance matrix estimation remains a concern. By using an antenna-based approach, we can improve conditioning by a factor of n_{ant} , but this is only one approach among many. Further work is needed to investigate which method, if any, proves optimal.

Chapter 4

Scientific Strategy

4.1 Science Goal

One of the key topics this thesis is observational cosmology with LOFAR & SKA pathfinders. This can be done in many ways - but this manuscript concerns itself primarily with the creation of large, deep and high-resolution surveys of the sky. While this approach is potentially extremely rewarding in terms of the science one can do with its resulting maps, it is also uniquely complicated.

Why, then, use this approach? One reason is, in fact, for the challenge itself. A high-resolution (matching HST resolution), wide-area (multiple degrees wide), high-quality radio survey has *never* been achieved at the time of writing. Many surveys of the radio sky exist, of course, but they tend to combine only two of those three qualities. FIRST(see Helfand et al. 2015), for example, has achieved tremendous results with a 4'' resolution, relatively low sensitivity, and no short baselines (thereby missing diffuse emission and extended structure). The VLASS (see Hales 2013) will aim to go to a 2.5'' resolution, medium sensitivity, and few short baselines.

In this context, a sky survey made using international LOFAR would be competitive until the SKA-MID survey (and considering it maps the Northern sky rather than the Southern sky, would arguably remain competitive even then). It would also allow LOFAR to fulfill the role of pathfinder in a very literal way, by providing datasets on which algorithms and imaging strategies could be tested before handling SKA data volumes.

Making a high-resolution full-sky survey using international LOFAR is thus arguably useful in and of itself in terms of interferometric techniques & instrumentation. What then of its science value? The two most obvious advantages of a good large-sky survey are that they are complete (i.e. they are an accurate sample of the underlying source distribution) while still giving information on rare outlier objects which may happen to lie in the field. This allows scientists a wealth of statistics from which to derive more robust estimations of population distributions and associated scientific measures of interest. Furthermore, depending on the quality of a given survey, it might even be able to provide such statistics simultaneously for various different fields of scientific interest.

Of course, LOFAR is already providing such catalogues - LOTSS [cite] is only the first of many to come. But these catalogues do not make use of the LOFAR international stations, and thus do not make full use of LOFAR's resolution (5'' resolution vs. 0.5''). Of course, the reason why this is so is because of the technical challenges introduced by the use of international stations. What would their use add to a LOFAR catalogue?

A high-resolution sky survey has all the advantages listed above, but with the strong benefit of also providing high-resolution images of everyone's favourite objects and sources. It allows for better optical matching and identification, which is particularly relevant e.g. when needing to associate either a low-z or high-z sources to optical counterpart sources (in the case of the Extended Groth Strip, for example, using the international stations means matching the Hubble Space Telescope's resolution). They therefore provide a much more useful contribution to multi-wavelength datasets. It also improves the image's sensitivity to compact sources embedded in diffuse emission: if the source is better-resolved, then the emission associated with compact sources is more easily separated from emission emitted by its surroundings. This can be of tremendous help in image interpretation. Finally, actually resolving objects allows scientists to have better morphological classification for compact objects, which can be extremely useful e.g. when interested in AGN populations vs star-forming galaxy populations.

talk about AGN science

talk about star-forming science

4.2 3C295 and the Extended Groth Strip

In this section, we briefly describe previous observations of the Extended Groth Strip, an extragalactic field with a rich multi-wavelength coverage described in Table 4.1. It has been long observed as part of the All-Wavelength Extended Groth Strip International Survey collaboration ((Davis et al. 2007)), which later became part of the CANDELS collaboration ((Grogin et al. 2011)). The field is centred at $\alpha = 14^h 17^m$, $\delta = +52^\circ 30'$, placing it between the tail of Ursa Major and Draco. Its size is $0.7' \times 0.1'$. It has notably been the subject of very deep Hubble Space Telescope observations, which the LOFAR VLBI imaging could attempt to match.

Telescope	Band	Resolution	Area
Chandra	X-ray	0.5'' – 6.0''	$17' \times 120'$
GALEX	UV	5.5''	1.25° diameter
HST/ACS	Optical	0.1''	$10' \times 67'$
HST/NICMOS	Optical	0.35''	0.0128 deg^2
Megacam	Optical	1.0''	1 deg^2
IRAC	IR	2.0''	$10' \times 120'$
Spitzer	IR	5.9'' – 19''	$10' \times 90'$
VLA	Radio	1.2'' – 4.2''	$30' \times 80'$

Table 4.1. Table recapitulating the multi-wavelength coverage of the Extended Groth Strip, with observations performed as part of the AEGIS (later, CANDELS) collaborations.

3C295 is a 3C¹ source, and thus one of the brighter sources in the Northern radio sky. It lies less than a degree away from the centre of the Extended Groth Strip, which has two important consequences: first, that it can potentially be used as a calibrator source for LOFAR; second, that unless well-modeled and subtracted at the observing instrument's maximum resolution, its sidelobes will pollute the EGS such that very little scientifically useful information might be recovered from a given observation.

4.3 Imaging the Full Primary Beam

Perform DID calibration at low resolutions (no international baselines) to get complete, approximatemodel of entire EGS field

4.4 Test Decorrelation

see effect of decorrelation on LOBOS sources around EGS as function of distance from 3c295 - talk about two sources of decorrelation (direction-dependent PSF, which is modelled, and gains changing with direction, which is unmodelled and will have an impact in image). See maximum impact of gain-decorrelation: we want flat decorrelation as function of distance from 3c295.

4.5 Imaging the EGS with LOFAR international stations

4.5.1 Science Goals

if decorrelation is merciful, proceed to patchwise imaging of EGS by using the results from the sections above (DI calibration using 3c295 model, followed by subtraction of all sources seen at low-res except within the patch we want to image; image, change patch; repeat until all EGS imaged)

¹Third Cambridge Catalogue of Radio Sources, a 1959 survey of the Northern radio sky

Chapter 5

High-resolution Imaging of 3C295

5.1 Aims & Methodology

Our aim in this section is to create a high-resolution model of 3C295, something that - as of yet - does not exist. More specifically, we seek to create a model that will allow us to find good phase-calibration solutions for LOFAR international baselines. While we also solve for amplitude gains, we know that we will need to correct the total source flux in each frequency subband as our initial spectral model is not necessarily correct. We select 6 sub-bands out of the total LOFAR HBA bandwidth, evenly spread throughout the bandwidth as shown in Fig. 5.1.

This approach should allow us to appropriately constrain the final spectral behaviour of our high-resolution model, once the amplitude correction is applied to ensure our model is compliant with pre-existing flux measurements for this source (Scaife & Heald 2012). [put image of source flux as function of frequency for 3c295, citing source and ideally showing position of our subbands]

Our procedure is as follows: we self-calibrate individual subbands, starting from a model extracted from a high-resolution VLA observation of 3C295 at 8.7 GHz (cf. Perley & Taylor 1991). Once this is done, we extract and apply a scalar flux correction factor for each subband so that the integrated flux of our 3C295 image is compatible with the existing literature at all frequencies. The resulting model is then reliable enough to calibrate our Groth Strip data using the full LOFAR array and the entire HBA bandwidth.

5.2 Data Reduction

5.2.1 Data & Observation Properties

The dataset used for this PhD project is part of the LOFAR Surveys KSP Tier-1 survey, which consists of a number of 8-hour pointing covering as much of the sky visible to LOFAR as possible. We analyse one of these pointings, an observation performed on the 28th of August 2014 and centred on the Extended Groth Strip. As part of the Tier-1 survey, it is an 8-hour-long observation. We limit ourselves to analysing only the HBA observation, meaning that we use 365 sub-bands which sample a total bandwidth of

[give bandwidth]. We use all Core and Remote LOFAR stations, as well as some of the International stations which were online at the time (specifically the German stations 1-5 and 7, along with the Swedish and the British station).

The data was acquired through the LOFAR Long-Term Archive, and is thus pre-processed and flagged for RFI using the standard tools ([cite aoflagger, ndppp?]).

5.2.2 Calibrating the Data

Since we plan on applying an amplitude correction based on the works of Scaife & Heald (see Scaife & Heald 2012), our overriding concern is to find good phase and amplitude gain without concern for the overall scaling factor. As such, our calibration strategy consists of calibrating 6 subbands, chosen across the LOFAR bandwidth, simultaneously. The chosen subbands, and their position in the total bandwidth, are shown here:

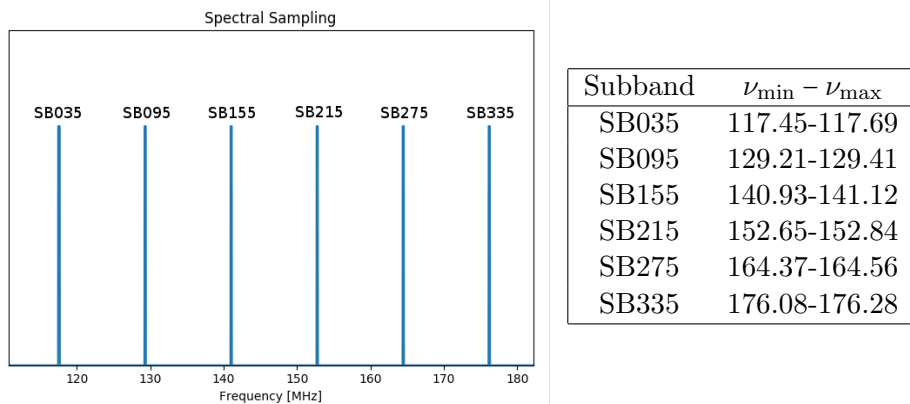


Figure 5.1. Position of subbands chosen across full LOFAR bandwidth

Table 5.1. Frequency bounds for the subbands chosen

Because no high-resolution models exist for 3C295 at our observing frequencies, which span quite a large bandwidth, care must be taken not to bias our model in an unphysical direction. We acquire the initial calibration model by extracting features from a NASA/IPAC Extragalactic Database¹ image of 3C295 (see Perley & Taylor 1991), shown in Fig. 5.2. This feature extraction is carried out using PyBDSM (Mohan & Rafferty 2015), changing all extracted Gaussians into points².

For SB035, the gain curves for all antenna when calibrating with the initial model are as shown in Fig 5.3. Note that, especially for the international baselines, the gain amplitudes show a lot of structure: this is unphysical, and represents the unmodelled flux being absorbed into the gain solutions.

¹<https://ned.ipac.caltech.edu/>

²This practice ensures that wrongly-estimated Gaussians do not end up introducing unphysical bias during calibration.

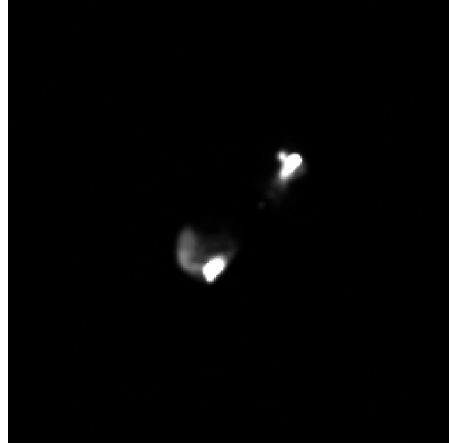


Figure 5.2. VLA observation of 3C295 at 8.7 GHz. Pixel size is 0.2''.

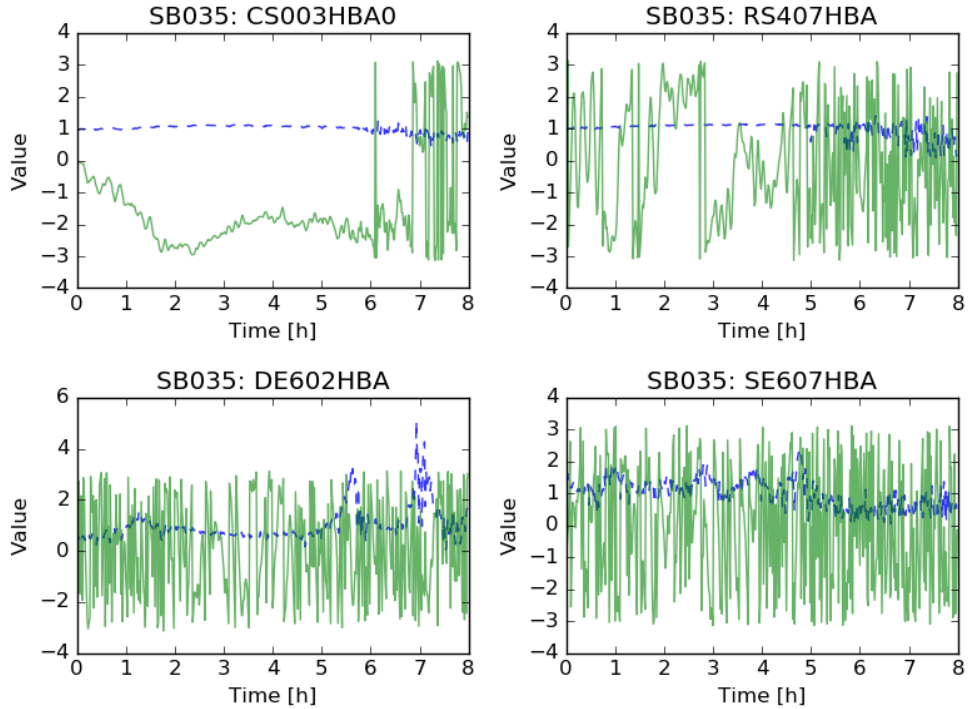


Figure 5.3. Gain curves for four LOFAR stations in SB035. Calibration was done using the VLA model. The blue curve shows the gain amplitude, while the green curve shows the phase. Here, only the values for the XX correlation are shown; they are indicative of the other Jones term properties.

A few features are immediately visible in Fig. 5.3. Firstly, we see in the gain amplitude curves of the core and remote stations that the gains for the last 2 hours of observation are noisier than the rest. This behaviour can be seen for most core and remote stations. Thankfully, the quality-based weighting schemes ought to optimise the contribution from these noisy visibilities, and so this is not too concerning. We see that the amplitude curves for the core and remote stations are nice and flat, with little structure to be

seen: this is very encouraging, as this is what we expect "physical" gain curves to look like. In other words, we see little pollution from unmodelled sources in the calibration model for core and remote stations. The phase seems reasonable, with some structure but not dominated by noise. Note that the phase is expected to wrap from $-\pi$ to π and vice-versa, which is what the fast oscillations in the last half of the phase gains of RS407HBA correspond to.

As for the international station gains, we see the presence of structure in the amplitude gain curve. This is indicative of the presence of sky model errors, which is expected: this is, after all, the gain curves after the first pass of calibration (i.e. without self-calibration). Very little information can be extracted from the phase curves, which wrap very fast: this is expected behaviour, as longer baselines rotate faster than shorter ones.

As calibration improves, however, we expect to get more of the true sky in our model. This, in turn, ought to decrease the structure in the gain curves. Fig 5.4 shows the gain curves for the same antennas after 3 passes of self-calibration.

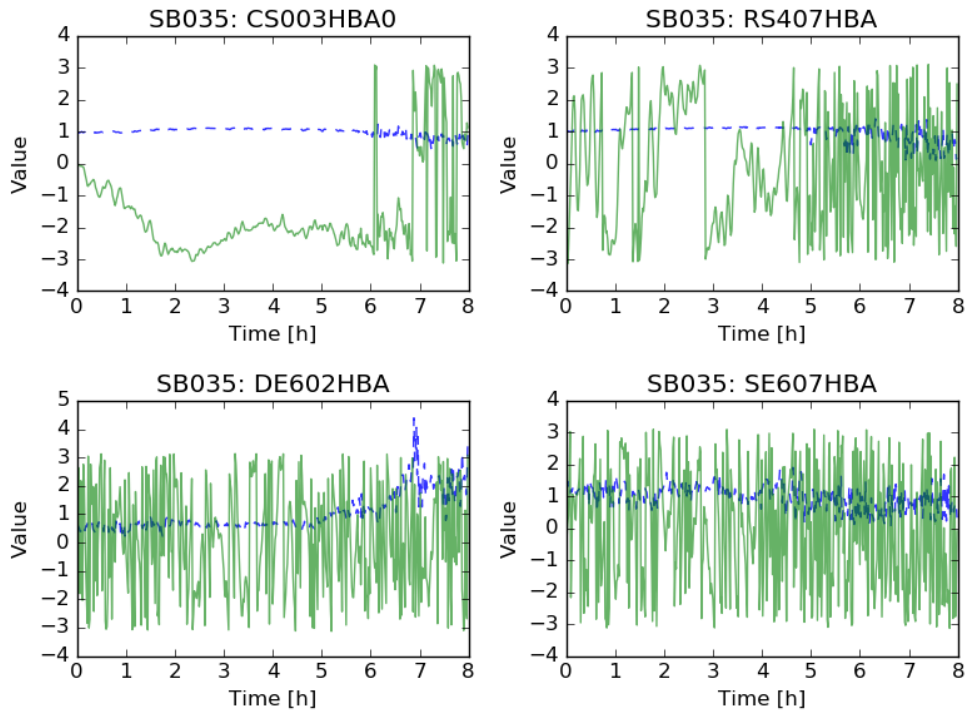


Figure 5.4. Gain curves for four LOFAR stations in SB035 after 3 passes of self-calibration. The blue curve shows the gain amplitude, while the green curve shows the phase. Here, only the values for the XX correlation are shown; they are indicative of the other Jones term properties.

As we can see, the last two hours remain noisy compared to the first two. What is interesting here is the evolution of the amplitude gain curves for DE602HBA and SE607HBA; while there is clearly still structure in the amplitude curves, we see that some of the structure is no longer present in the curves. What this indicates is that

the sky model has improved compared to what it had been, but there is still room for improvement: indeed, this is as expected, as there are many more sources than 3C295 within the primary beam.

This self-calibration was performed over all 6 subbands simultaneously; this allowed us to constrain the flux distribution in the sky as a function of frequency, even though the absolute scale in each image is known to be wrong. The absolute scale distribution being wrong is no issue, however; indeed, for each given subband, the gains are all wrong by the same multiplicative factor. This factor changes between subbands, however, and so the corrected visibilities must be corrected by the appropriate multiplicative factor for the true position-dependent spectral indices to be found. Mathematically, we have:

$$\mathbf{V}_{pq}^{\text{corr.}}(t, \nu) = (a_{\text{false}}(\nu) \tilde{\mathbf{G}}_{p,t}^\nu)^{-1} \mathbf{V}_{pq}^{\text{meas.}}(t, \nu) (a_{\text{false}}(\nu) \tilde{\mathbf{G}}^\nu)^{-1} \quad (5.1)$$

$$\mathbf{V}_{pq}^{\text{meas.}}(t, \nu) = (a_{\text{true}}(\nu) \mathbf{G}_{p,t}^\nu) \mathbf{X}_{pq}(t, \nu) (a_{\text{true}}(\nu) \mathbf{G}_{p,t}^\nu) \quad (5.2)$$

where uppercase, boldface letters denote 2×2 Jones matrices, and lowercase letters are scalars. Here, $a_{\text{false}}(\nu)$ is the incorrect scaling factor applied at frequency ν by calibrating without the proper spectral indices for all the components of 3C295, while $a_{\text{true}}(\nu)$ is the correct scaling factor. The true scaling factor is known from low-resolution calibrator analysis, while the false scaling factor is an arbitrary function of frequency. Assuming that our estimate for the Jones matrices is accurate (modulo the scaling factor), i.e. that $\tilde{\mathbf{G}}_{q,t}^\nu \approx \mathbf{G}_{q,t}^\nu$, then

$$(a_{\text{false}}(\nu) \tilde{\mathbf{G}}_{p,t}^\nu)^{-1} (a_{\text{true}}(\nu) \mathbf{G}_{p,t}^\nu) = \frac{a_{\text{false}}(\nu)}{a_{\text{true}}(\nu)} (\tilde{\mathbf{G}}_{p,t}^\nu)^{-1} \mathbf{G}_{p,t}^\nu \quad (5.3)$$

$$\approx \frac{a_{\text{false}}(\nu)}{a_{\text{true}}(\nu)} \mathbf{I} \quad (5.4)$$

and so

$$\mathbf{V}_{pq}^{\text{corr.}}(t, \nu) \approx \left(\frac{a_{\text{false}}(\nu)}{a_{\text{true}}(\nu)} \right)^2 \mathbf{X}_{pq}(t, \nu) \quad (5.5)$$

we can thus recover the properly-scaled visibilities in each subband by normalising the visibilities (i.e. divide by whatever a_{false} happens to be with a given calibration at a given frequency) and subsequently scaling them by a_{true} so that the average value in the corrected visibilities is equal to what's expected at this frequency.

Having calibrated our 6 subbands with the VLA model, we deconvolve them simultaneously. This allows us to improve the conditioning of the imaging inverse problem. After three passes of self-calibration, we have a spectral cube with 6 frequency slices centred on the various subbands. The stacked residual images are in Fig 5.5, before and after self-calibration. We see that noise falls by a factor of 1.17. Note that this measure is not as significant as might be expected: indeed, since the scaling factors for each subband is arbitrary, the overall decrease in noise could be attributed to a single subband, should its incorrect scaling factor dominate. The overall decrease is nevertheless encouraging. The frequency-dependent model is shown in Fig. 5.6. Note that while there is some frequency-dependent flux distribution changes, it is very small.

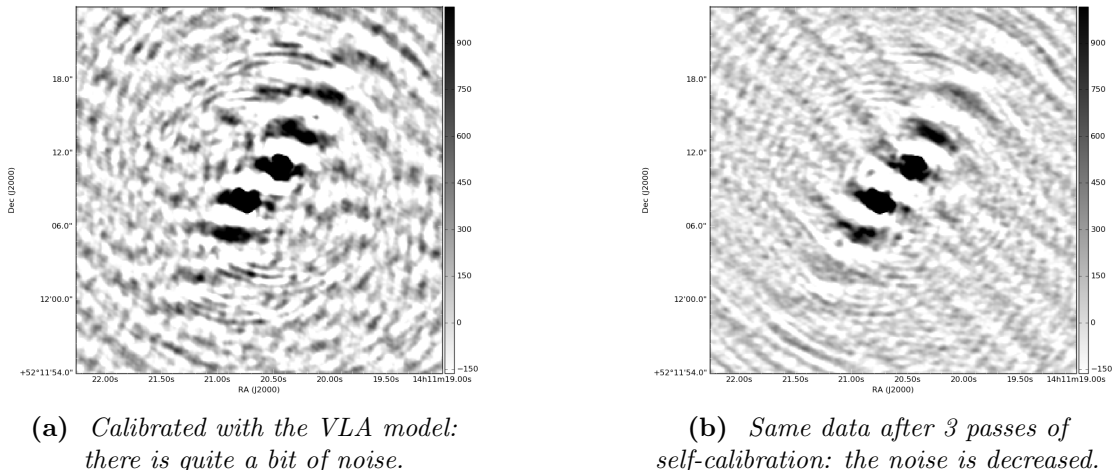


Figure 5.5. Images made with 6 subbands spread across the LOFAR bandwidth.

!!! SHOW GAIN CURVES, LOTS OF PLOTS ETC

!!! ANALYSE CONVERGENCE OF CALIBRATION ACROSS SUBBANDS

apply beam to account for different sensitivities of different baselines

use full-Jones solver (i.e. solve for a 2x2 complex matrix) to account for effects such as Faraday rotation etc

!!! SHOW JONES CHAIN WE SOLVE FOR AND EXPLAIN IT, MATHS ETC: ***B*J** for Beam*Jones

!!! SHOW DIRECTION-DEPENDENT PSF EFFECT WHICH WE MODEL

5.3 Overlays & Spectral Analysis

5.3.1 Overlays of 3C295 at Multiple Frequencies

Show overlays of our low-freq model onto images of 3c295 at various other freqs - VLA, optical, IR, X-ray, etc.

Comment on behaviour of various components, astrometric accuracy, etc

5.3.2 Spectral Analysis

Work with Astron guy to extract spectral behaviour of various components of 3C295 over multiple wavelengths, since he's got a purpose-built package

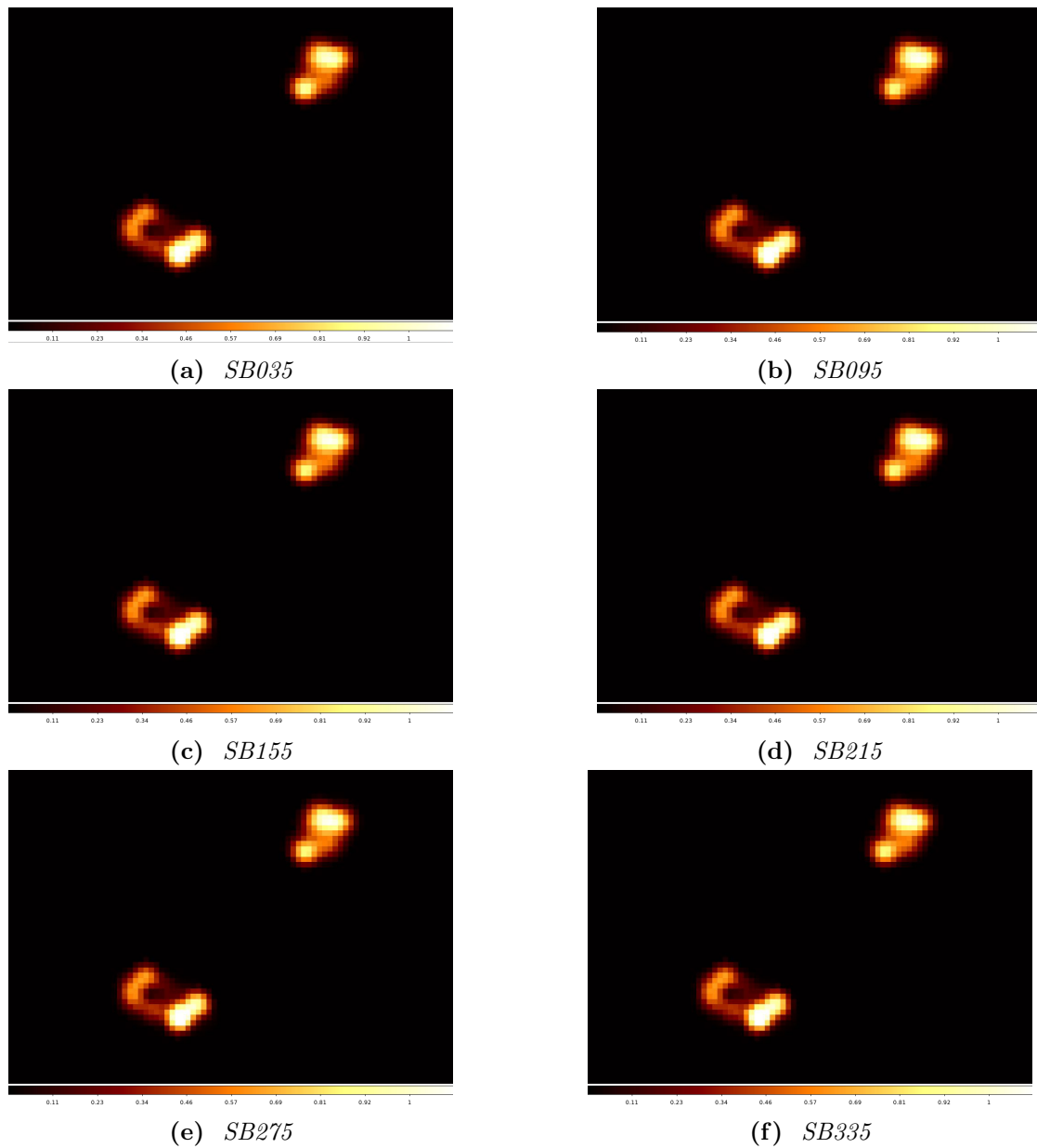


Figure 5.6. Source model for each subband after 4 passes of self-calibration.

Chapter 6

Imaging the Extended Groth Strip without International Stations

6.1 Aims & Methodology

Here, we want to make wide-field image of entire LOFAR primary beam, centred on EGS, *at once*. Such image never been done in this freq. band

This requires direction-dependent calibration, which in turns requires good direction-independent calibration starting from good model of 3C295. This is because this source is brightest in primary beam, and its sidelobes will dominate in the image unless properly subtracted

Source extraction using model made from this low-res image will allow us to subtract neighbouring sources when imaging the EGS at high res.

Technical limitations in computing means that maximum attainable image size (in number of pixels) will limit pixel resolution to 5" (actual number to be determined properly!) - this in turn means that the international stations are not useful for imaging, as the resolution they allow will not be reachable due to these technical, computational limits.

methodology: calibrate full LOFAR bandwidth using high-res model from section above, done using the LOFAR Surveys KSP pipeline (talk about DD calibration, facetting, etc) finally, overlays of sources in the field compared with VLA, optical, etc

6.2 Data Reduction

6.2.1 Data & Observation Properties

same as before, same dataset

6.2.2 Calibration Strategy

start w/ D.I. calibration using model from before.

follow with D.D. calibration w/ lofar pipeline - describe the pipeline and its properties

show self-cal loop (before-after) in images & gains; show improvement from direction-dependent cal. on entire field & individual sources

6.3 Overlays & Images

show overlays of various radio sources in the field over their optical, IR, X-ray, etc counterparts. Discuss astrometric accuracy, calibration quality, morphology, etc etc

Chapter 7

Imaging the Extended Groth Strip with the full LOFAR array

7.1 Aims & Methodology

primary aim: see if direction-independent calibration of EGS good enough, for international baselines, to allow for HR imaging of entire EGS with acceptable upper bounds to decorrelation throughout field.

in other words: can entire EGS be placed on same facet as 3C295 at high resolutions?
Link to V.

necessary test: investigate impact of decorrelation as function of distance from 3C295 (calibrator) - do we lose enough signal to lose resolution?

LOBOS survey gives list of VLBI phase calibrators in primary beam: compact sources, should show impact of direction-dependent gain errors directly. These are distributed at various distances from 3C295, conveniently.

Show images (+ overlays?) of direction-dependent PSF (i.e. modelled decorrelation due to time-freq averaging) and images of LOBOS sources

Finally, show plot of ratio of $flux_{peak} / flux_{integrated}$ as function of distance from 3C295: the flatter, the better.

Imaging strategy: image the field patch by patch.

Have source list of entire EGS from section V. Use that to subtract all source save those in the patch from visibilities, then image (self-cal?) over that patch. Rinse and repeat throughout EGS.

7.2 Testing Decorrelation - LOBOS Sources in the Primary Beam

describe LOBOS catalogue & sources chosen - why, how

#	RA [hms]	Dec [dms]	Dist. from EGS [deg.]	Dist. from 3C295 [deg.]
1	14:30:18.72	52:17:29.80	2.041	2.904
2	14:19:44.44	54:23:04.58	1.928	2.517
3	14:21:20.05	53:03:46.00	0.864	1.743
4	14:21:09.41	51:22:32.46	1.294	1.728
5	14:11:50.32	52:49:02.66	0.844	0.619
6	14:11:20.23	52:12:04.30	0.915	0.000
7	14:08:07.00	52:55:11.36	1.409	0.869
8	14:08:09.76	52:44:46.56	1.354	0.680

Table 7.1. Table recapitulating the positions of all 8 chosen calibrator sources, along with their distance from the observation phase centre (EGS phase centre) and calibrator phase centre (3C295), respectively.

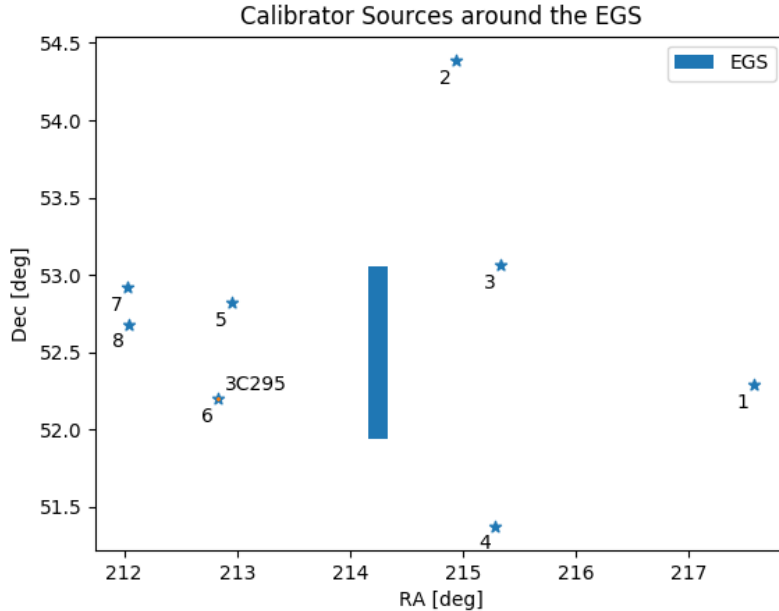


Figure 7.1. Position of the calibrator sources around the EGS. Note that this is not projected properly onto the celestial sphere.

show images of decorrelation, residuals etc for all 8 sources

7.3 Patchwise Imaging of the EGS using LOFAR International Stations

Chapter 8

Conclusion & Future Work

Lorem ipsum dolor sit amet, consectetur adipiscing elit. Morbi vehicula dui vel sem elementum viverra. Nullam molestie egestas finibus. Vestibulum at rhoncus massa, ac mollis nulla. Nam vitae vestibulum ex. Interdum et malesuada fames ac ante ipsum primis in faucibus. Curabitur lobortis quam eget dui pretium pulvinar. Quisque consequat dapibus justo, eu blandit lacus auctor id. Vivamus vestibulum diam id feugiat posuere. Morbi ut vehicula urna, id laoreet turpis. Nam dignissim magna augue, et rhoncus felis lacinia nec. Praesent convallis ultrices hendrerit.

Praesent porta lacus est. Duis tempor augue augue, ac pharetra nisi viverra sed. Integer tristique risus ac metus aliquam, in pretium felis porttitor. Sed eu ipsum vitae tortor faucibus ultrices. Cras sem erat, eleifend eget massa et, dapibus vulputate velit. Duis semper non odio in semper. Mauris quis massa rhoncus ante ullamcorper faucibus. Nam quis sollicitudin diam. Maecenas et posuere augue, ac aliquam sapien. Curabitur ac tristique ante. Sed tempor tellus a magna vehicula fringilla. Suspendisse arcu lacus, bibendum vitae velit vel, posuere commodo ipsum. Suspendisse et congue sem. Maecenas maximus quam sed interdum dignissim. Etiam ac tempor risus. Quisque vel nisi arcu. Nunc consectetur, nisl nec blandit egestas, dolor felis tincidunt odio, et iaculis lacus nunc in sem. Suspendisse potenti. Aenean est ante, egestas ac nulla eu, suscipit maximus orci. Etiam suscipit neque sed diam hendrerit, eu iaculis risus laoreet. Sed venenatis ultricies justo porta placerat. Quisque ac convallis nunc. Suspendisse et risus enim.

Bibliography

- Briggs, D. S. 1995, in Bulletin of the American Astronomical Society, Vol. 27, American Astronomical Society Meeting Abstracts, 1444
- Davis, M., Guhathakurta, P., Konidaris, N. P., et al. 2007, ApJ, 660, L1
- Fried, D. L. 1978, Journal of the Optical Society of America (1917-1983), 68, 1651
- Grobler, T. L., Nunhokee, C. D., Smirnov, O. M., van Zyl, A. J., & de Bruyn, A. G. 2014, MNRAS, 439, 4030
- Grogin, N. A., Kocevski, D. D., Faber, S. M., et al. 2011, ApJS, 197, 35
- Hales, C. A. 2013, ArXiv e-prints
- Hamaker, J. P., Bregman, J. D., & Sault, R. J. 1996, A&AS, 117, 137
- Helfand, D. J., White, R. L., & Becker, R. H. 2015, ApJ, 801, 26
- Jennison, R. C. 1957, in IAU Symposium, Vol. 4, Radio astronomy, ed. H. C. van de Hulst, 159
- Jennison, R. C. 1958, MNRAS, 118, 276
- Joardar, S., Bhattacharyya, S., Bhattacharya, A., & Datta, C. 2010, Progress In Electromagnetics Research B, 22, 73–102
- Kazemi, S. & Yatawatta, S. 2013, MNRAS, 435, 597
- Kellerman, K. & Sheets, B. 1984, Serendipitous discoveries in radio astronomy : proceedings of a workshop held at the National Radio Astronomy Observatory, Green Bank, West Virginia on May 4, 5, 6 1983
- Mohan, N. & Rafferty, D. 2015, PyBDSF: Python Blob Detection and Source Finder, Astrophysics Source Code Library
- Noordam, J. E. & Smirnov, O. M. 2010, A&A, 524, A61
- Pearson, T. J. & Readhead, A. C. S. 1984, ARA&A, 22, 97
- Perley, R. A. & Taylor, G. B. 1991, AJ, 101, 1623
- Rau, U. & Cornwell, T. J. 2011, A&A, 532, A71
- Rogers, A. E. E., Cappallo, R. J., Hinteregger, H. F., et al. 1983, Science, 219, 51

- Rogers, A. E. E., Hinteregger, H. F., Whitney, A. R., et al. 1974, ApJ, 193, 293
- Scaife, A. M. M. & Heald, G. H. 2012, MNRAS, 423, L30
- Smirnov, O. M. 2011a, A&A, 527, A106
- Smirnov, O. M. 2011b, A&A, 527, A107
- Smirnov, O. M. 2011c, A&A, 527, A108
- Smirnov, O. M. 2011d, A&A, 531, A159
- Smirnov, O. M. & Tassee, C. 2015, MNRAS, 449, 2668
- Tassee, C. 2014, ArXiv e-prints
- Tassee, C., Hugo, B., Mirmont, M., et al. 2017, ArXiv e-prints
- Thompson, A. R., Moran, J. M., & Swenson, Jr., G. W. 2001, Interferometry and Synthesis in Radio Astronomy, 2nd Edition
- van Cittert, P. H. 1934, Physica, 1, 201
- Yatawatta, S. 2014, MNRAS, 444, 790